Investigating the Martian soil at the InSight landing site

Pierre Delage, Bernardo Caicedo, Matt Golombek, Tilman Spohn, Cédric Schmelzbach, Nienke Brinkman, Eloise Marteau, Naomi Murdoch, Nicholas Warner, Véronique Ansan, et al.

To cite this version:

Pierre Delage, Bernardo Caicedo, Matt Golombek, Tilman Spohn, Cédric Schmelzbach, et al.. Investigating the Martian soil at the InSight landing site. Soils and Rocks, 2024, Deformation Characteristics of Geomaterials, 47 (3), pp.e2024005023. 10.28927/SR.2024.005023 . hal-04470316

HAL Id: hal-04470316
https://hal.science/hal-04470316v1

Submitted on 21 Feb 2024

Soils and Rocks
An International Journal of Geotechnical and Geoenvironmental Engineering
www.soilsandrocks.com
ISSN 1980-9743
ISSN-e 2675-5475

Investigating the Martian soil at the InSight landing site

Pierre Delage[1#], Bernardo Caicedo[2#], Matt Golombek[3], Tilman Spohn[4], Cédric Schmelzbach[5], Nienke Brinkman[5], Eloise Marteau[3], Naomi Murdoch[6], Nicholas Warner[7], Véronique Ansan[8], Bruce Banerdt[3], Juan-Pablo Castillo-Betancourt[1], Pascal Edme[5], Annabel Gomez[9], Matthias Grott[4], Ken Hurst[3], Mark Lemmon[10], Philippe Lognonné[11], Sylvain Piqueux[3], Johann Robertsson[5], David Sollberger[5], Simon Stähler[5], Nicolas Verdier[12], Christos Vrettos[13], Nathan Williams[3]

Review Article

Keywords
Mars
Regolith
Seismometer
Heat probe
Elastic parameters
Mechanical properties

Abstract

The InSight mission is a geophysical mission aimed at better understanding the structure of Mars and of the other rocky planets of the solar system. To do so, a lander accommodating two cameras, a very sensitive seismometer, and a dynamic self-penetrating heat probe nicknamed the mole were placed on the Mars surface by the Instrument Deployment Arm (IDA). Besides geophysical data (which definitely enriched the existing knowledge on the structure of Mars), the InSight instruments significantly increased the knowledge of the geological and geotechnical characteristics of the surface material at the InSight site. Small strain (elastic) parameters were derived from wave velocity measurements during the hammering sessions between the self-penetrating probe and the seismometer. A detailed observation of the soil profile along a depth of 37 cm was made possible thanks to the photos taken by the cameras, and to a detailed analysis of the mole penetration process. Further information was provided by an intense campaign of scraping and piling conducted by the IDA on the surface sand/dust layer. It was shown that the soil profile was composed of a surface 1 cm thick sand/dust layer, overlaying an around 20 cm thick loose duricrust made up of a cohesive matrix containing some pebbles, located above a 12 cm layer of sand overlaying a gravel/sand deposit. It is believed that the geology and soil mechanics data provided by the InSight mission will help for further robotic exploration of Mars.

1. Introduction

Mars is one of the four rocky planets of the Solar system, with a Martian year as long as around two times the Earth year, an average diameter of 6779 km (0.553 that of the Earth) and, as a result, a smaller gravity of 3.721 m/s^2. The atmosphere on Mars is mainly composed of CO_2 with an average atmospheric pressure of 610 Pa. As a consequence, the surface on Mars is submitted to wind, with significant consequences on the surface deposits, both in terms of particle shape and surface morphology.

[#] Corresponding authors. E-mail address: pierre.delage@enpc.fr; bcaicedo@uniandes.edu.co
[1] Ecole des Ponts ParisTech, Centre National de la Recherche Scientifique, Laboratoire Navier, Marne la Vallée, France.
[2] Universidad de los Andes, Bogota, Colombia.
[3] California Institute of Technology, National Aeronautics and Space Administration, Jet Propulsion Laboratory, Pasadena, California, USA.
[4] DLR Institute of Planetary Research, Berlin, Germany.
[5] ETH Zürich, Institute of Geophysics, Department of Earth Sciences, Switzerland.
[6] Institut Supérieur de l'Aéronautique et de l'Espace, Toulouse, France.
[7] The State University of New York, Department of Geological Sciences, Geneseo, NY, USA.
[8] Nantes Université, Laboratoire de Planétologie et Géodynamique, Centre National de la Recherche Scientifique, Nantes, France.
[9] California Institute of Technology, Pasadena, CA, USA.
[10] Space Science Institute, Boulder, CO, USA.
[11] Université Paris Cité, Institut de Physique du Globe de Paris, Centre National de la Recherche Scientifique, Paris, France.
[12] Centre National d'Études Spatiales, Toulouse, France.
[13] Technische Universität Kaiserslautern, Department of Civil Engineering, Kaiserslautern, Germany.

Submitted on May 12, 2023; Final Acceptance on December 26, 2023; Discussion open until November 30, 2024.

https://doi.org/10.28927/SR.2024.005023

The InSight mission on Mars (Interior Exploration using Seismic Investigations, Geodesy and Heat Transport) is a geophysical mission aimed at better understanding the structure of Mars and of the other rocky planets of the solar system (Banerdt et al., 2020). The mission, managed by NASA with European Space Agencies (e.g. CNES, France and DLR, Germany) is based on using a lander accommodating various instruments.

Besides geophysical data, that definitely enriched existing knowledge on the structure of Mars, some of the InSight instruments that interacted with the soil significantly enlarged the knowledge of the geological and geotechnical characteristics of the surface soil at the InSight site, that may also be useful for future robotic exploration of Mars. The data on the soil behaviour gained during the InSight mission are presented in this paper.

2. The InSight mission

The InSight lander, that landed at the surface of Mars in western Elysium Planitia on 26 November 2018, is represented in Figure 1 (this date corresponds to sol 1, sol is the name of a Martian day). The artist view accommodates various instruments, including a very sensitive seismometer called SEIS (Seismic Experiment for Interior Structure), comprising a very-broad-band seismometer (VBB) funded by CNES, and a short-period (SP) one developed at Imperial College (Lognonné et al., 2019). In the Figure, SEIS is covered by a white hemispherical wind and thermal shield (WTS).

The lander also included a low-velocity penetrator – nicknamed the Mole - as part of the Heat flow and Physical Properties Package HP^3 (Spohn et al., 2018, 2022a, b). The package was provided by the German Aerospace Center (DLR) through its Institute of Planetary Research. The probe is 40 cm long and 2.7 cm in diameter. The HP^3 was designed to measure the thermal conductivity and the thermal gradient down to 3-5 metres below the surface. The heat flow from the interior of the planet can be calculated as the product of the thermal conductivity and the temperature gradient and provides important constraints on the composition and the evolution of the planet. To do so, the mole was supposed to drag a Kapton® tether to depth equipped with temperature sensors positioned to optimize the gradient measurement (Spohn et al., 2018). Further details on the penetration process of the mole are given in Section 5.2.

Figure 2a (Golombek et al., 2020a) shows an image of the InSight lander, heat shield and parachute taken on 6 December 2018 from the HiRISE (High Resolution Imaging Science Experiment) camera on board the Mars Reconnaissance Orbiter (MRO). More details are also given for the heat shield (b), lander (c) and parachute (d). The 20 m radius dark spot around the lander corresponds to the surficial dust layer that has been expelled around by retrorockets during landing. Its extension to the southeast is due to prevailing wind direction from the northwest in this area, confirmed by the InSight instruments later on. The photo also provides more information about the landing site, with circular impact craters at various degradational states, due to wind and aeolian

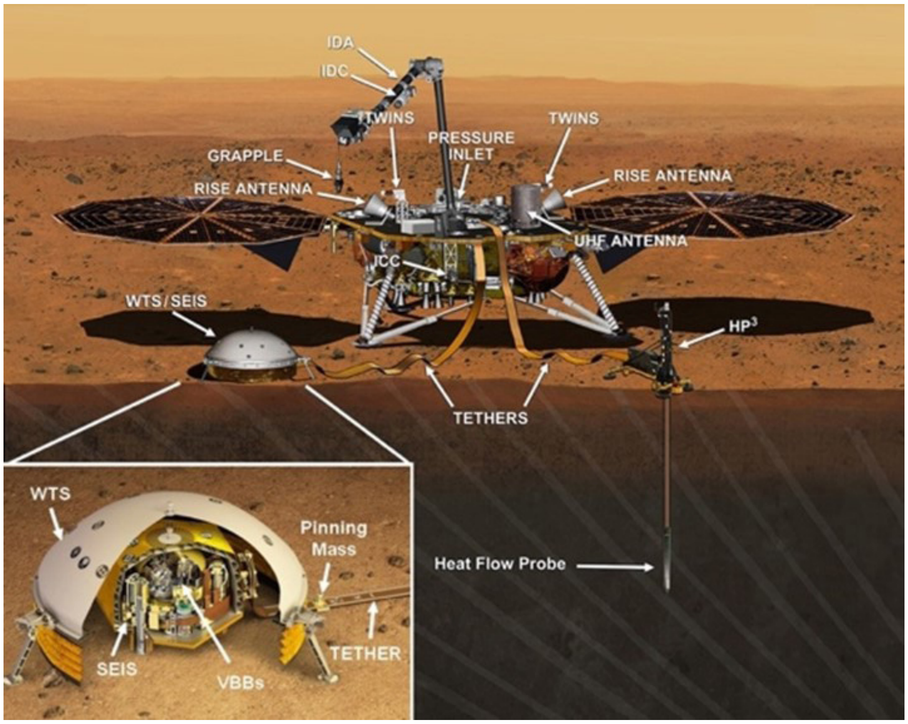

Figure 1. Artist view of the InSight lander and of the SEIS seismometer (image credit: JPL-NASA and IPGP D.Ducros).

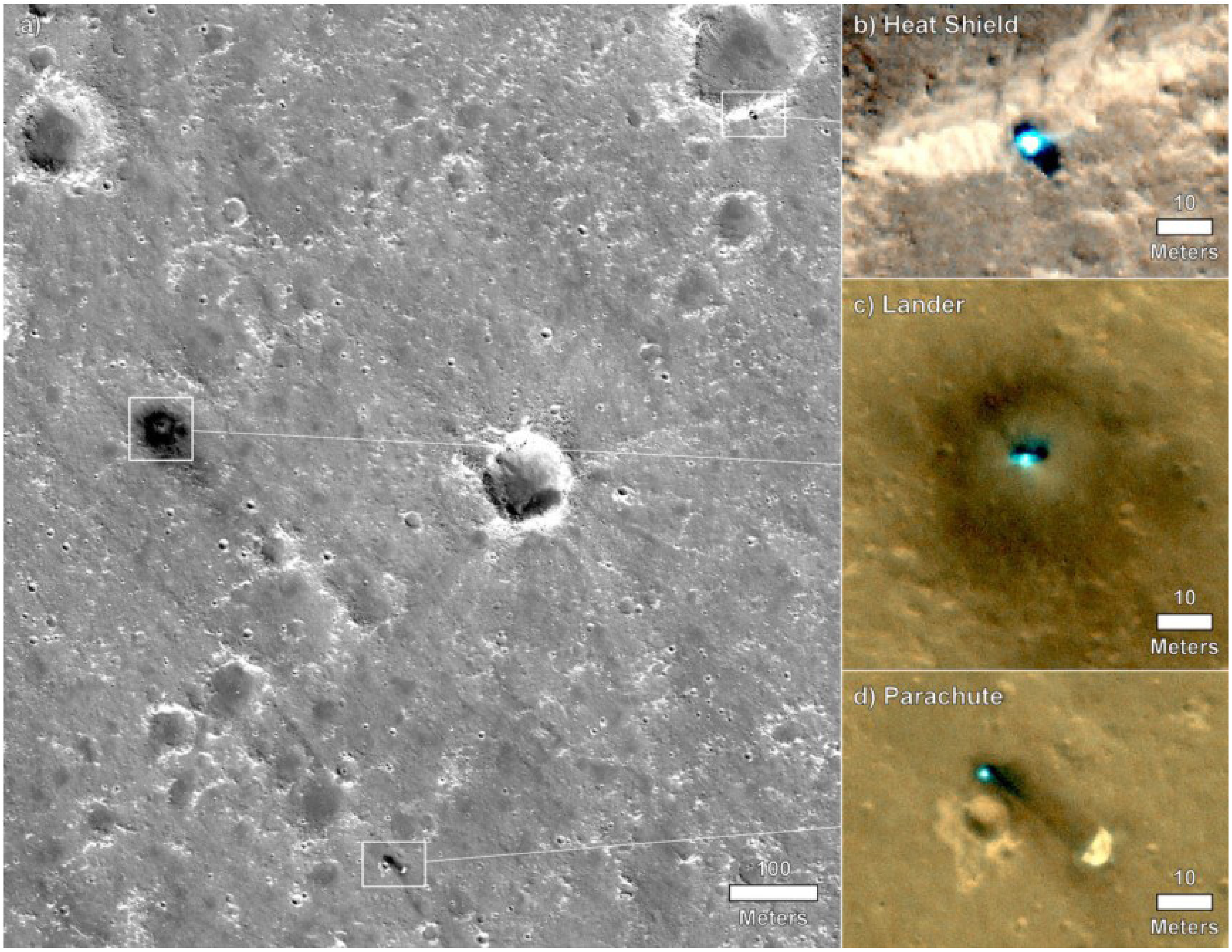

Figure 2. HiRISE image from the InSight landing site taken from the Mars Reconnaissance Orbiter: (a) General view; (b) Heat shield; (c) Lander; (d) Parachute (Golombek et al., 2020a).

transportation of surface particles. A relatively fresh crater is observed at 400 m to the east of the lander.

The SEIS and HP^3 instruments have been placed on the surface of Mars thanks to the grapple located at the end of the 2 m long Instrument Deployment Arm (IDA) of the lander (Trebi-Ollennu et al., 2018). The IDA (see Figure 1) also accommodates a scoop that can be used for pushing on the surface and scraping and pouring regolith (Golombek et al., 2023). Direct visual observation of the soil around the lander is made possible by two cameras, the wide-angle Instrument Context Camera (ICC), placed on the lander and the Instrument Deployment Camera (IDC), with a better resolution, fixed on the IDA (Figure 1). The lander includes two solar arrays (2.2 m diameter, 700 W each on clear days when clean) that provide energy to the lander and instruments. Energy is transmitted to the SEIS and HP^3 by tethers that also transmit data. Among other instruments, the lander accommodates a meteorological station continuously monitoring wind and temperature (Banfield et al., 2018), a magnetometer and a precision tracking system (Folkner et al., 2018).

The ICC photo of Figure 3, taken at the beginning of the mission (early 2019), shows on the left-hand side the HP^3 support structure (dark in shadow) containing the mole prior to penetration in the soil. One also sees the SEIS covered by the white hemispherical (clean) WTS. The distance between them is close to 1.18 m. The Figure also provides a view of the landing area, that was selected to be flat, with low rock abundance and mainly composed of sandy regolith (Golombek et al., 2017).

Figure 4, extracted from the Mars Orbiter Laser Altimeter (MOLA) shaded topographic map of Mars (Golombek et al., 2018), shows the landing sites of InSight (NSY) in Elysium Planitia, together with those of i) the Viking Lander 2 (VL2, 1976) in Utopia Planitia, ii) of the Mars Science Laboratory (MSL) Curiosity rover in Gale crater (2012) and iii) of the Mars Exploration Rover (MER) Spirit in Gusev crater (2004). InSight landed on ~200 m thick lava flows from Early Amazonian-Hesperian period (1.8 - 3.6 billion years) (Golombek et al., 2018, 2020a), underlain by sedimentary rocks of likely Noachian age (around >3.6 billion years, Pan et al., 2020) possibly containing phyllosilicates. The

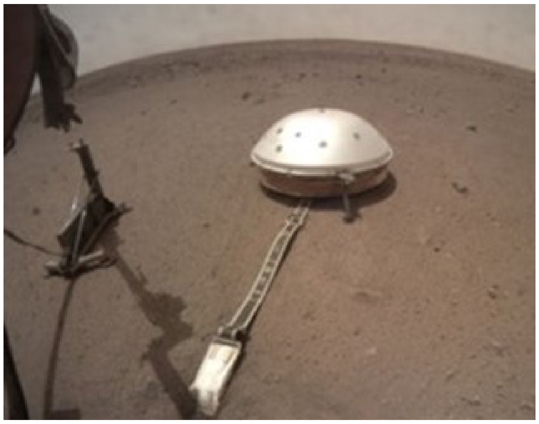

Figure 3. Image taken from the Instrument Context Camera (ICC) on sol 87 (local time 11:54:07 LMS) showing the location of SEIS and of the HP^3 support structure, 1.18 metre apart from each other (image credit: JPL/NASA).

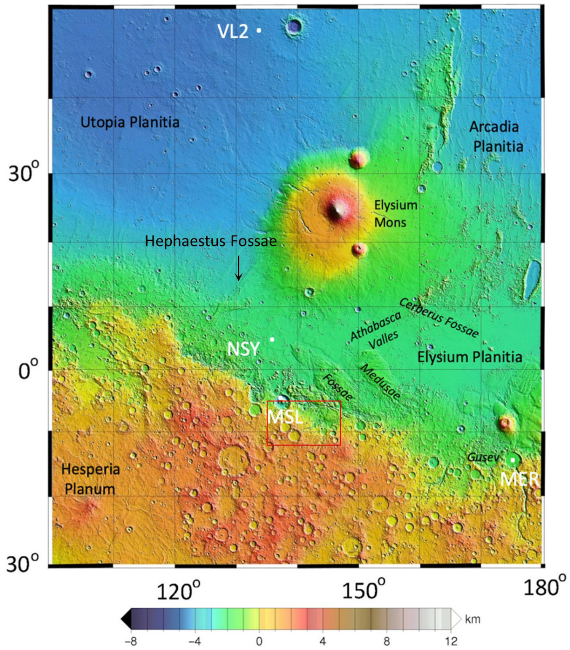

Figure 4. Locations of the InSight lander (NSY) close to the equator (4.502°N/135.623°E), not far from the dichotomy boundary that separates, on Mars, the southern heavily cratered older highlands from the northern lowlands (see colour scale). The map is a portion of the Mars Orbiter Laser Altimeter (MOLA) shaded topographic map of Mars (after Golombek et al., 2020a).

Figure also shows Mars' dichotomy, with the northern hemisphere (mainly in blue, corresponding to a – 4 km altitude) at lower elevation than the southern hemisphere (red colour is + 3.5 km). The southern hemisphere is much more heavily cratered (older) than the northern plains.

Figure 5 shows an ICC photo taken in Autumn 2022 after 4 years of mission. The photo shows that all devices are covered by a dust layer that also covered the solar arrays, finally reducing the energy production. As a consequence, the mission ended on 15 December 2023 for lack of energy.

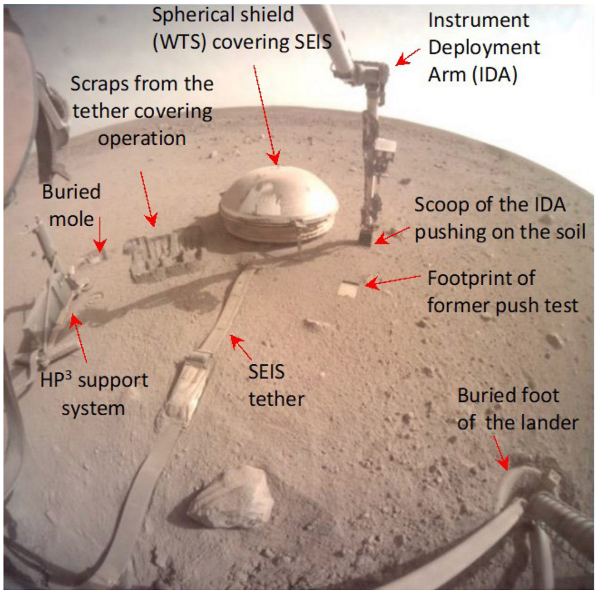

Figure 5. Image taken by the Instrument Context Camera on sol 1170 showing the SEIS WTS (diameter 720 mm) with the Instrument Deployment Arm (IDA) vertically pushing on the soil at the right of the SEIS. As described in more details in Section 5.3.2, the IDA is performing the second elastic pushing experiment, resulting in a tilt monitored by SEIS. The rectangular imprint of the back of the scoop is from the indentation and first elastic experiment. All instruments are covered by a dust layer progressively brought by the Martian winds (image credit: NASA-JPL).

In the Figure, the IDA (Golombek et al., 2023) is pushing on the regolith surface in an attempt to further identify the elastic parameters of the surface thanks to the tilt detected by SEIS, as will be commented in Section 5.3.2. A flat footprint made by a former push test by the IDA can also be observed. The HP^3 support system is to the left of the SEIS and the location where the mole is buried (from which the support system has been removed, see below) is indicated. Some scraps made by the IDA scoop to cover the SEIS tether by pouring regolith from the scoop for a better thermal insulation and for cleaning the solar arrays can also be seen at the left of the WTS (Golombek et al., 2023). The WTS is also covered by dust, except in the zone where the regolith has been poured on it, resulting in a cleaner white section.

3. The geology of the InSight landing site

The investigation of the surface deposits on Mars has been considered in detail since the landing of Vikings 1 and 2 in 1976 (e.g. Moore & Jakosky, 1989). It has afterwards been completed by data from landers and rovers of other missions. Global thermal inertia (see Section 4.1) and albedo measurements of Mars along with surface investigations by nine landers and rovers show that Mars is covered by a surface layer of generally fine-grained materials that is metres thick (Christensen & Moore, 2008; Golombek et al., 2008). These materials have been mostly modified by mass

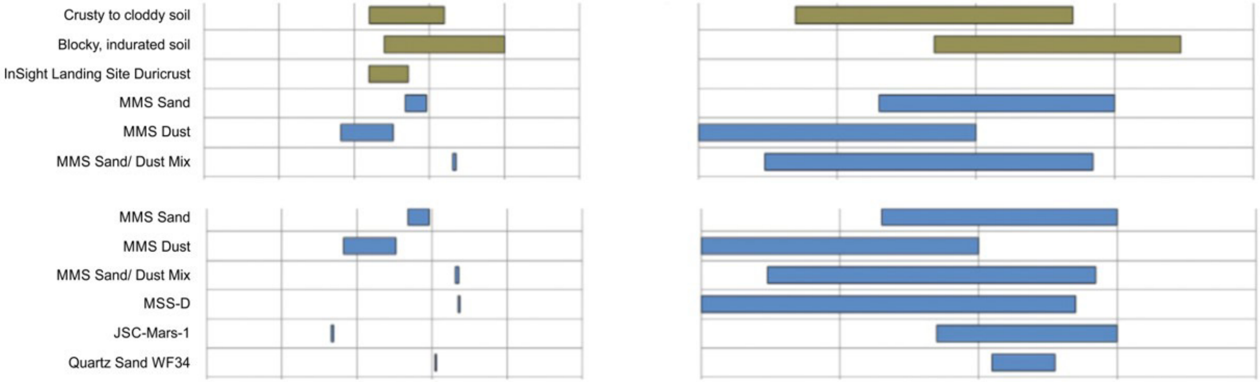

Figure 6. Various soils observed at the surface of Mars, after Spohn et al. (2022b), based on compilations from Golombek et al. (2008) and Herkenhoff et al. (2008).

wasting, aeolian and impact processes. All of the landers and rovers obtained information about the surface materials at their landing sites and along rover traverses using cameras (some high-resolution), arms and scoops, drills and rock abraders, and rover wheels. Most of the soils encountered are composed of dominantly sand size materials with some cohesion (Christensen & Moore, 2008; Herkenhoff et al., 2008). The sand is basaltic in composition, mostly 0.05 to 0.3 mm diameter (very fine to fine sand) and individual grains are generally equant to very equant and subrounded to rounded (Yen et al., 2005; Goetz et al., 2010; McGlynn et al., 2011, 2012; Minitti et al., 2013; Ehlmann et al., 2017) suggesting an origin via impact and aeolian activity (McGlynn et al., 2012; Golombek et al., 2020d).

A synthesis of the soils observed on Mars is presented in Figure 6, in which a distinction is made between i) drift materials, observed at surface and made up of very small particles between 1 and 10 µm with densities between 1000 kg/m^3 and 1300 kg/m^3, sand (between 1100 kg/m^3 and 1300 kg/m^3), crusty to cloddy soil and blocky, indurated soils.

At the InSight landing site, the granular regolith results from the long-term and successive impacts of meteors into the lava flows of Elysium Planitia, that progressively broke the basalt parent rock into smaller and smaller rocks and particles, that are afterwards submitted to erosion and sorting by gravity and winds, to end up with a sand-like surface regolith (Golombek et al., 2017). Estimates of the regolith thickness is schematically represented in Figure 7, where two impacts are represented (Warner et al., 2017; Golombek et al., 2020d). When the impact takes place only in the regolith (left hand side of the Figure, smaller impactors), the ejecta around the crater is only composed of regolith. When the impactor comes in contact with the bedrock (right hand side, bigger impactors), rocks are present in the ejecta around the crater.

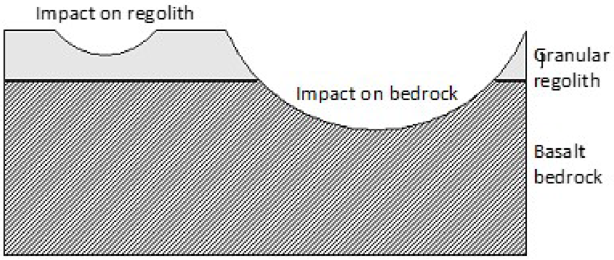

Figure 7. Schematic representation of the regolith formation from impacts (with impactor coming at 5 km/s) either touching the bedrock (right hand side, larger impactors), with blocky ejecta around the crater, or only touching the regolith (left hand side), with no blocky ejecta around the crater.

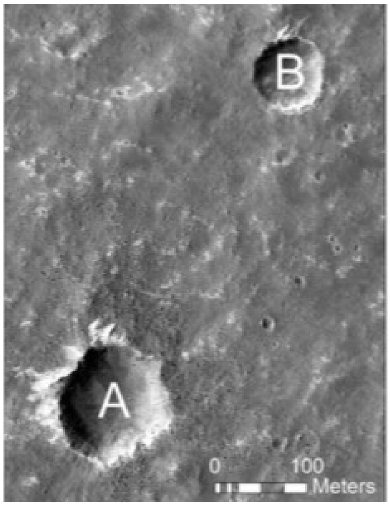

Figure 8. HiRISE image showing fresh crater A (112 m diameter), with rocky ejecta around and B (75 m) with no rocky ejecta around. The depth at which ejecta is sourced in fresh craters is 0.084 times the diameter (Golombek et al., 2017). Note that Warner et al. (2017) and Golombek et al. (2020c) have a more specific treatment of the regolith depth.

This can be seen in the photo of Figure 8, taken from the HiRISE (High Resolution Imaging Science Experiment) camera on board the Mars Reconnaissance Orbiter (MRO). The fresh crater A is 112 m diameter with rocky ejecta around (little black dots), whereas fresh crater B (75 m diameter) has no rocky ejecta. Given that the depth at which ejecta is sourced in fresh craters is 0.084 times the diameter, the image indicates that the bedrock depth is larger than 0.084 × 75 = 6.3 m and smaller than 9.4 m. This was an important criterion for site selection (Golombek et al., 2017), since it was planned during the mission to penetrate the HP^3 thermal probe down to 5 m.

Aeolian activity (motion of small particles by the wind) is common on Mars, with some active dunes and ripples. At InSight, aeolian bedforms are rare, with some ripples near relatively fresh impact craters (e.g. Figure 8). The ripples are dusty, suggesting relative inactivity (Golombek et al., 2020a) and a surface with little aeolian activity except for wind vortices that produce little net motion of grains in the modern era (Charalambous et al., 2021; Baker et al., 2021).

The stratigraphy is illustrated by the HiRISE photo of Figure 9, showing a steep scarp of Hephaestus Fossae exposure (see location in Figure 4), a fracture ~900 km northwest of the InSight landing site that cuts through a potentially analogous terrain (Warner et al., 2017, 2022; Golombek et al., 2018). The photo shows ~4-5 m thick, relatively fine-grained regolith overlying blocky ejecta that grades into strong, jointed bedrock. Given that the bedrock is composed of basalt lava, the regolith is mainly basaltic as well.

The image analysis carried out on Figure 10 (Warner et al., 2022) shows the profile of the steep scarp with, on top, a 4-5 m thick granular layer (with a maximum slope of 20°, smaller than the angle of repose estimated at 30°), underlain by a 13-29 m thick boulder-dominated cliff-forming unit, underlain by another cliff-forming unit (112-133 m thick) that may be the primary bedrock, with a talus at its base inclined at 32° (close to the estimated angle of repose of loose granular materials, see Delage et al., 2017). The estimation of the grain distribution of the talus material is not straightforward, but it is probable that it is composed from part of fine regolith that flowed down from the top, together with other rocky debris with size comprised between 1 m and 10 m coming from the upper layer of blocky ejecta. The entire stratigraphic sequence is consistent with an impact-comminuted lava plain with a gardened regolith that is up to 10 metres thick. The regolith fines upwards is a result of the higher frequency of small (order of 1 to 10 m) impacts.

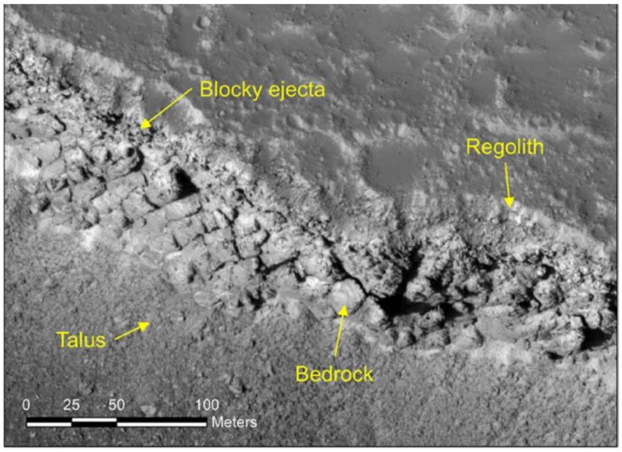

Figure 9. A portion of the exposed steep scarp of Hephaestus Fossae in southern Utopia Planitia (Golombek et al., 2018).

4. Physical and mechanical data from previous investigations

Some physical properties of the regolith at the landing site, estimated prior to landing, either from orbiter measurements of from lab testing on regolith simulants, are now presented.

4.1 Thermal inertia

The main information about the nature of the surface soil gained from orbiters is the thermal inertia *I*, that is used to estimate the average grain size of surface sandy deposits. Thermal inertia (unit $Jm^{-2}K^{-1}s^{-1/2}$) is given by:

$$I = \sqrt{k \rho c_p} \qquad (1)$$

where k is the thermal conductivity, ρ the density, and c_p the specific heat capacity of the material. The principle that allows derivation of average particle size from thermal inertia is simple: for the same mass, the changes in temperature of a particle

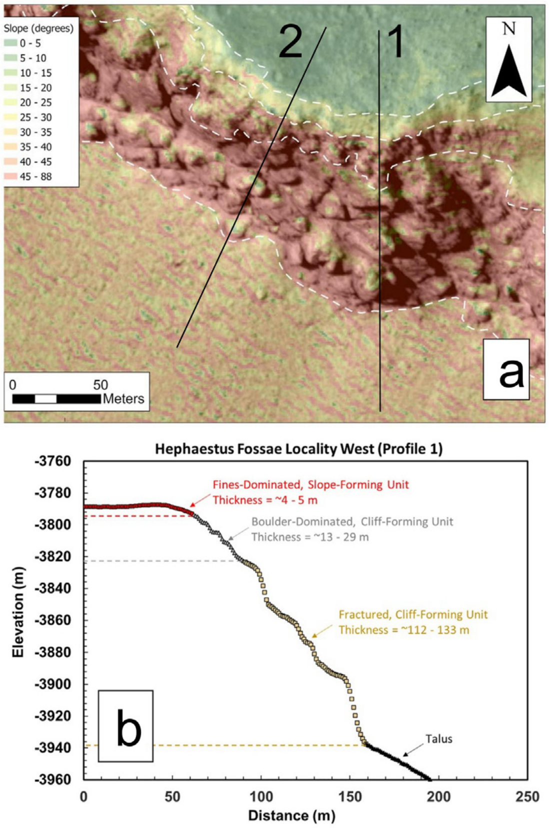

Figure 10. (a) HiRISE image of the Hephaestus Fossae exposure, a fracture ~900 km northwest of the InSight landing site (see Figure 4); (b) Slopes determined along profile 1 (Warner et al., 2022).

(the average temperature of the atmosphere on Mars changes as much as 100 °C between days and nights) are slower for larger particles (small specific surface) and faster for small particles (high specific surface). Note however that inter-grains cementation in slightly cohesive granular materials may increase the thermal inertia. While density and specific heat capacity vary little for different soils, thermal conductivity can vary by orders of magnitude, depending on bulk porosity, composition, grain size and the state of cementation or induration.

Figure 11 shows a colour map of thermal inertia values characterised around the InSight landing site by the THEMIS (Thermal Emission Imaging System) instrument on board of the Mars Odyssey spacecraft launched in 2001 (e.g., Palluconi & Kieffer, 1981; Mellon et al., 2000; Putzig & Mellon, 2007; Golombek et al., 2008).

The image in Figure 11 shows an area of relatively constant thermal inertia, in accordance with what is observed around the lander (see Figure 3). Orbital thermal inertia measurements indicated values between 160 J m^{-2} K^{-1} s$^{-1/2}$ and 230 J m^{-2} K^{-1} s$^{-1/2}$ (Golombek et al., 2017), which were later confirmed by local measurements using the InSight HP^3 Radiometer (Spohn et al., 2018; Golombek et al., 2020a; Mueller et al., 2021; Piqueux et al., 2021). The average grain size derived from this value is around 170 µm. In Figure 11, high thermal inertia data are in red. Some red dots can be observed in rocky ejecta craters with I around 300 J m^{-2} K^{-1} s$^{-1/2}$ (craters A, B), comparable with what can be directly observed in Figure 8.

4.2 Wave velocities and elastic properties of regolith simulants

A previous estimation of wave velocities at surface was helpful to interpret the surface wave data recorded by SEIS. To do so, a laboratory investigation of wave velocities was carried out in the laboratory, prior to the mission, on various regolith simulants. The selection of a relevant Martian regolith simulant (Seiferlin et al., 2008) is not an easy task. In the case of InSight, four simulants have been studied to match the range of parameters expected on Mars (Golombek et al., 2008, 2017; Herkenhoff et al., 2008, see Figure 6). These simulants, often considered for missions on Mars, are the Mojave Mars Simulant (MMS, Peters et al., 2008), the Eifelsand and the MSS-D (Mars Soil Simulant-D) simulants (see Delage et al., 2017), together with a fourth simulant, the Fontainebleau sand (NE34). Compared to the first three that were too angular, the Fontainebleau sand is a well sorted sub-rounded to rounded sand, preferable to reflect the mechanical effects of long-term saltation on the grains of Martian surface regoliths. A detailed description of the MMS simulant, of the Eifelsand and MSS-D simulants are given in Delage et al. (2017). The Fontainebleau sand, located in the Fontainebleau Forest near Paris, France, is almost exclusively composed of hyaline quartz (Andria-Ntoanina, 2011).

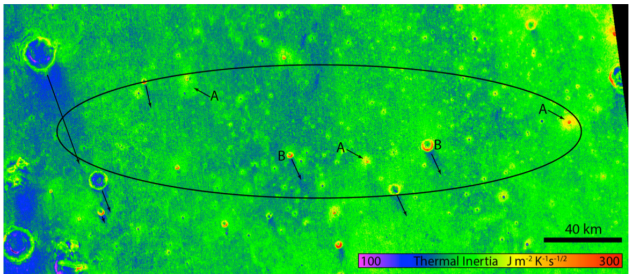

Figure 11. Thermal inertia values at the InSight landing site (Golombek et al., 2017).

The grain size distribution (GSD) curves of the four simulants, presented in Figure 12, indicate that the GSD of MSS-D is clearly bi-modal (with both a 50% sand fraction - larger than 100 µm - and a 50% fraction of fine-grained crushed olivine, smaller than 100 µm in the silt size range). The GSDs of MMS and Eifelsand simulants are somewhat comparable, with however a greater percentage of smaller particles in the Mojave simulant. The Fontainebleau sand has a smaller average grain diameter D_{50} = 220 µm, a little bit larger than the 170 µm estimated value at the InSight site. The sand is quite well sorted around its mean diameter, with a uniformity coefficient C_u = 1.57.

The seismic velocities were measured by using bender elements inserted in top and bottom of triaxial specimens and able to generate and receive both shear and compression waves. The size of the specimen for the MMS, Eifel and MSS-D simulants was 50 mm in diameter and 100 mm in height. These simulants were tested from low to high confining stresses (i.e. 20 to 500 kPa), with densities of 1670 kg/m^3 for MSS-D, 1550 kg/m^3 for MMS, and 1350 kg/m^3 for Eifelsand (Delage et al., 2017). When testing the Fontainebleau sand (Castillo-Betancourt et al., 2023), one tried to better replicate the Mars conditions of low density and low stresses. A larger cylindrical specimen (100 mm in diameter and 170 mm in height) was used to have a longer wave travel path. To achieve a low density, the pluviation technique (Kolbuszewski, 1984) was used with very small fall height, allowing a low value of dry density of about 1400 kg/m^3, corresponding to a density index I_d of 6%. To minimize stress and have a homogeneous stress field, bender elements

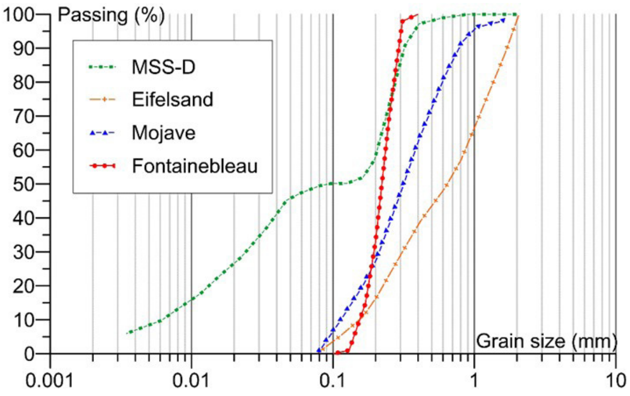

Figure 12. Grain size distribution of the Martian simulants.

measurements were carried out on horizontal samples, with careful calibration of stresses due to the membrane and to self-weight. Stress was changed by applying vacuum to the sample, up to 80 kPa. Bender measurements could be carried out at stress as low as 1 kPa (with however more dispersion in this stress range), enlarging at low values the range of stress generally considered in geotechnical engineering. The travel time was determined by using the common peak-to-peak approach, as shown in Figure 13. The Figure also shows the interaction between both *P* and *S* waves: some slight perturbation is observed in the *S* wave when the *P* wave first arrives and the same holds for the *P* wave at arrival of the *S* wave.

Figure 14 shows the evolution of the *P* and *S* wave velocities with respect to the effective isotropic confining stress *p*. In a standard fashion, the increase in velocity is non linearly related to the increase in intergranular forces resulting from the increase of confining stress. For the three simulants tested at higher stresses (i.e. Mojave, Eifel and MSS-D, Delage et al., 2017), the compression wave velocity increased from approximately 250 m/s at 25 kPa to around 600 m/s under 500 kPa. The measurements were carried out at lower stress in the Fontainebleau sand, down to 2.6 kPa (Castillo-Betancourt et al., 2023) with a value of 110 m/s, increasing to 360 m/s at 80 kPa, close to the values of the Mojave and Eifelsand simulants. A good comparability between those three simulants is observed, whereas the data of the finer MSS-D simulant are distinct, with larger velocities. The data also provide an estimation of the velocities at surface, close to 110 m/s for V_p and 70 m/s for V_s.

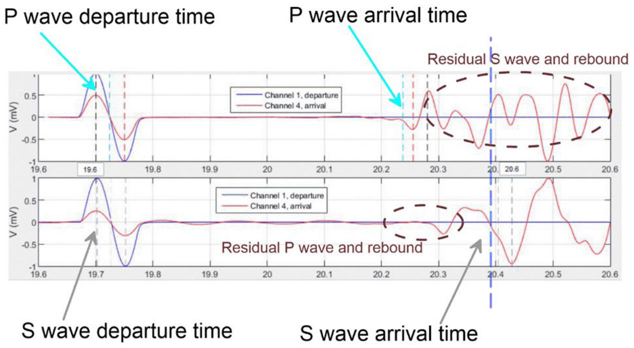

Figure 13. Peak-to-peak approach and S-wave arrival (Castillo-Betancourt et al., 2023).

The changes in seismic velocities with respect to the confining stress *p* are defined by an empirical power law (e.g. Santamarina et al., 2001), as follows:

$$V_p = \alpha_p \left(\frac{p}{1\text{kPa}}\right)^{\beta_p}, \; V_s = \alpha_s \left(\frac{p}{1\text{kPa}}\right)^{\beta_s} \tag{2}$$

in which parameters α_i and β_i are experimentally determined; α_i is the velocity under 1 kPa confinement.

As recalled by Santamarina et al. (2001), the stiffer the particles and the denser the packing, the higher the value of α and the lower the β exponent. Note that theoretical values of β are 1/6 for Hertzian contacts between elastic spherical spheres, 1/4 for cone-to-plane contacts (typical of rough or angular particles) and 1/4 for spherical particles with yield. As shown in Figure 6, the values reported for sands by Santamarina et al. (2001) are between 0.12 and 0.28, with a linear relationship between β_s and α_s. Interestingly, our values are in line with Santamarina's et al. (2001) data (Figure 15).

The measurements of V_p and V_s make it possible to calculate the Poisson's ratio (ν) over the studied range of stresses using the following equation:

$$V_p / V_s = \sqrt{\frac{2(1-\nu)}{(1-2\nu)}} \tag{3}$$

giving:

$$\nu = 0.5\frac{(V_p / V_s)^2 - 2}{(V_p / V_s)^2 - 1} \tag{4}$$

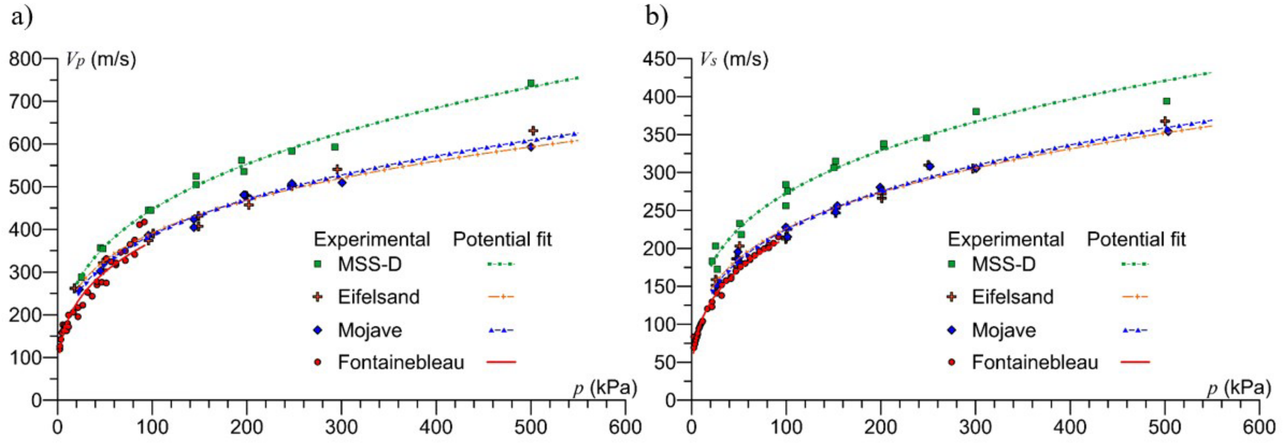

Figure 14. Compressive wave velocity of the four simulants: (a) Compression waves V_p; (b) Shear waves V_s.

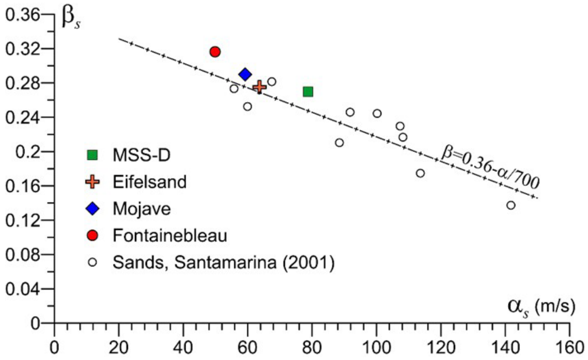

Figure 15. Values of α_s and β_s of sands and the tested regolith simulants (see Equation 2).

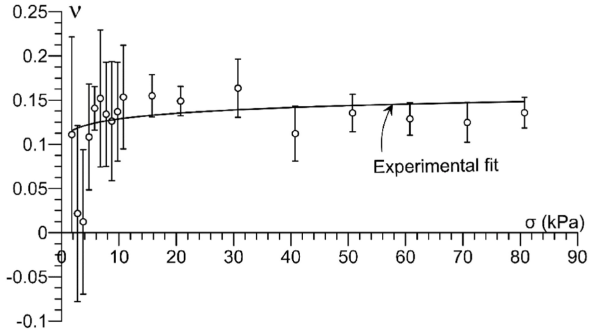

Figure 16. Poisson's ratio calculated for the wave velocities measured on Fontainebleau sand (Castillo-Betancourt et al., 2023).

As shown in Delage et al. (2017), comparable values of ν around 0.22 were obtained for the three simulants investigated (MSS-D, Eifelsand and Mojave). Conversely, a smaller value around 0.14, with no significant change with respect to stress above 10 kPa, was determined for the Fontainebleau sand, as seen in Figure 16. This is in agreement with the data obtained in-situ by Bachrach et al. (2000) on a beach sand. The change of ν at low stresses (< 5 kPa) is more difficult to characterise, due to significant dispersion in a zone where the bender elements become less operational. Further investigation is needed in this zone of low stresses.

Knowing V_p, V_s and the density also allows to determine the Young's modulus E, according to the following expression:

$$E = \rho {V_p}^2 \left(\frac{3 - 4/\left(V_p/V_s\right)^2}{\left(V_p/V_s\right)^2 - 1} \right) \tag{5}$$

The changes in Young's modulus for the four simulants investigated are presented in Figure 17.

In a standard fashion, the modulus increases with the confining stress (Jamiolkowski, 2012). The curves also indicate an order of magnitude of the Young's modulus at low stress at surface, with values around 20 MPa for the Fontainebleau sand (for which smaller stresses have been considered in the experimental investigation), a little bit larger for the other simulants. Note that this value is in good agreement with those derived from a small strain investigation of the interaction between the foot of the SEIS seismometer and loose samples ($\rho = 1400$ kg/m^3) of Fontainebleau sand (Delage et al., 2022).

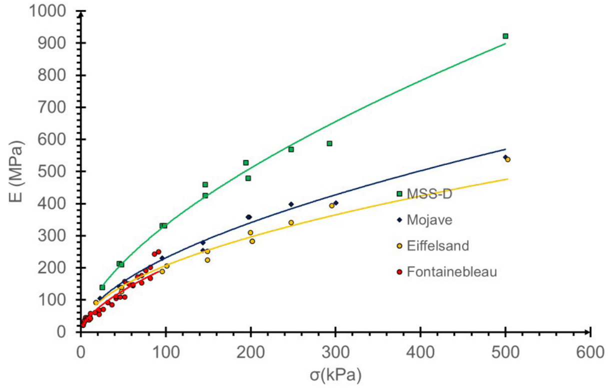

Figure 17. Changes in Young's modulus with respect to the confining stress.

Since roughness effects at the inter-grains contact are suspected to be more significant at low stresses like in the case of Mars, a detailed analysis based on the mechanics of contacts has been carried out by Caicedo et al. (2023) based on the works of Bachrach et al. (2000), Bahrami et al. (2005) and Butt et al. (2015). Figure 18 shows the changes in wave velocity with respect to stress for the Fontainebleau sand. They are no longer based on a semi-empirical power law like in Figure 14, but result from the contact theory with an average roughness parameter σ_{rms} between 0.6 µm and 0.8 µm (a little bit larger than the 0.2 µm identified by Atomic Force Microscopy on a Fontainebleau sand grain, see Caicedo et al. 2023). Based on Bachrach et al. (2000), Figure 18b presents the changes in Poisson's ratio with stress obtained with a fraction ξ of non-slipping grains between 0.55 and 0.65, with best fit for ξ = 0.6. The Figure also shows that the Poisson's ratio is constant down to 5 kPa, whereas the dispersion at low stress does not allow to draw a conclusion on a possible decrease below.

5. Direct determination of the regolith properties

5.1 Direct observations at surface

Direct observation of the regolith particles on Mars has been made by the microscopic imagers of the Spirit, Opportunity (McGlynn et al., 2011) and Curiosity rovers, the Phoenix lander and by the atomic force microscope of the Phoenix mission (Pike et al., 2011). They revealed sorted dark grey basaltic sub-rounded to rounded fine sand particles due to wind saltation, with diameter between 80 and 200 µm, as seen in Figure 19 from the Phoenix mission (Goetz et al., 2010). This range is compatible with the average diameter (170 µm) derived from thermal

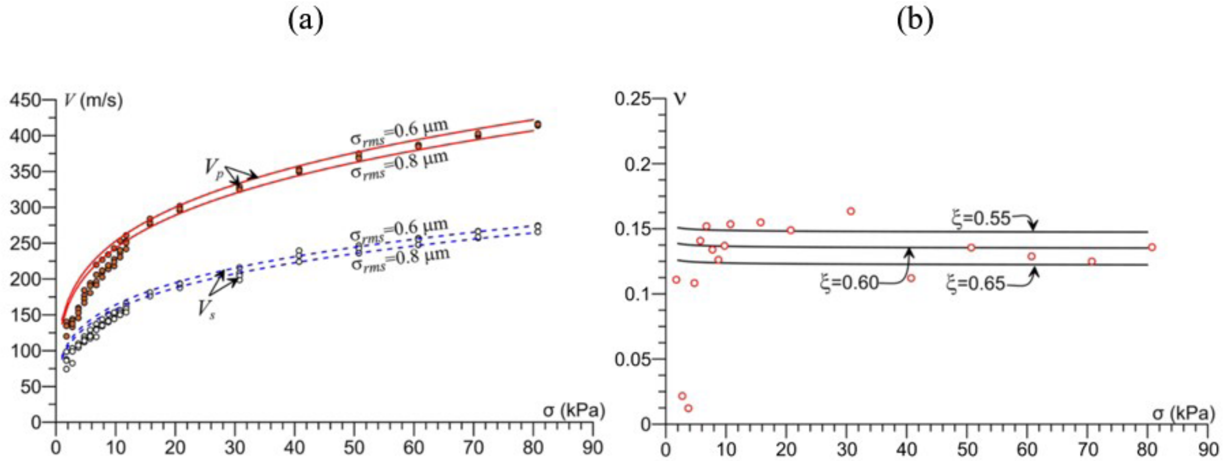

Figure 18. (a) Comparison between the theoretical contact model and test data on Fontainebleau sand (σ_{rms} is the asperity parameter); (b) Changes in Poisson's ratio with stress (ξ is the fraction of non-slipping grains, Caicedo et al., 2023).

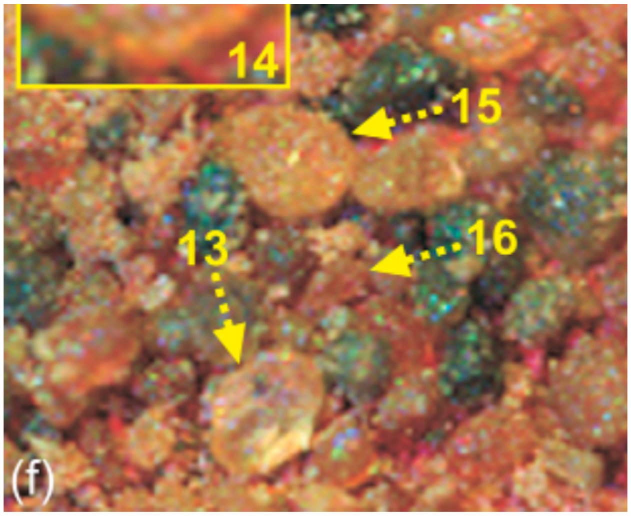

Figure 19. Microscopic observation of sub-rounded to rounded particles of Mars regolith at the Phoenix site. Picture width is 500 µm (Goetz et al., 2010).

inertia measured at the InSight landing site. Bright red dust particles (2-5 µm) of slightly chemically altered basalt are also observed (Arvidson et al., 2008, 2009, Goetz et al., 2010).

The colour of the particles in Figure 19 varies from dark grey (black) to slightly reddish. This probably depends on the degree of contamination of their surface by red fines, or on surface stains (Goetz et al., 2010).

Figure 20 shows the walls of the various pits (P1, P2 and P3) formed during the excavation of the surface by the rocket exhaust beneath the lander during landing. It provides some information on the true nature of the regolith at the InSight landing site. The Figure shows that, in fact, the soil is not a well sorted subrounded to rounded (cohesionless) sand, as suggested from thermal inertia measurements (further observations - see more details later on - indicated that this is however true for the 1 cm surface layer). One observes in the Figure, along the 10 - 12 cm height of the steep pit walls, a more resistant layer having enough cohesion to allow the static stability of the walls (and the stability with respect to the rocket exhaust, which would probably require a much larger cohesion). Note that the layers of crust and duricust could be cemented by salts deposited by thin films of water via interactions of atmospheric water vapour and soils, as suggested by chemical measurements by Viking and Mars Exploration Rover spacecraft (Banin et al., 1992, Haskin et al., 2005, Hurowitz et al., 2006). The effects of rocket exhaust are quite localized, with an average pit diameter of 50 cm. One observes, on the eroded walls ~ centimetre-size pebbles embedded in a finer cohesive grain matrix. Observation of pits (*Pi*) and of other excavations (*di*) also show some larger black angular likely basaltic pebbles.

5.2 Mechanical and thermal data from the self-penetrating HP^3 device

The Heat Flow and Physical Properties Package HP^3 was planned to measure the temperature profile and a thermal conductivity profile down to a depth of 3-5 m, together with related physical properties. The temperatures would have been measured using sensors on a Kapton tether which a small self-penetrating device (the mole) would have dragged down to the targeted depth (Spohn et al., 2018). Pausing penetration at depth intervals of 50 cm, a thermal conductivity profile would have been measured using sensors embedded in the mole (e.g., Grott et al., 2019; Spohn et al., 2018) and thermal diffusivity would have been determined using the temperature sensors on the tether. From the product of the temperature gradient and the thermal conductivity, the heat flow from the interior of Mars would have been calculated (provided that a minimum depth be reached to avoid perturbance caused by seasonal variations of the surface

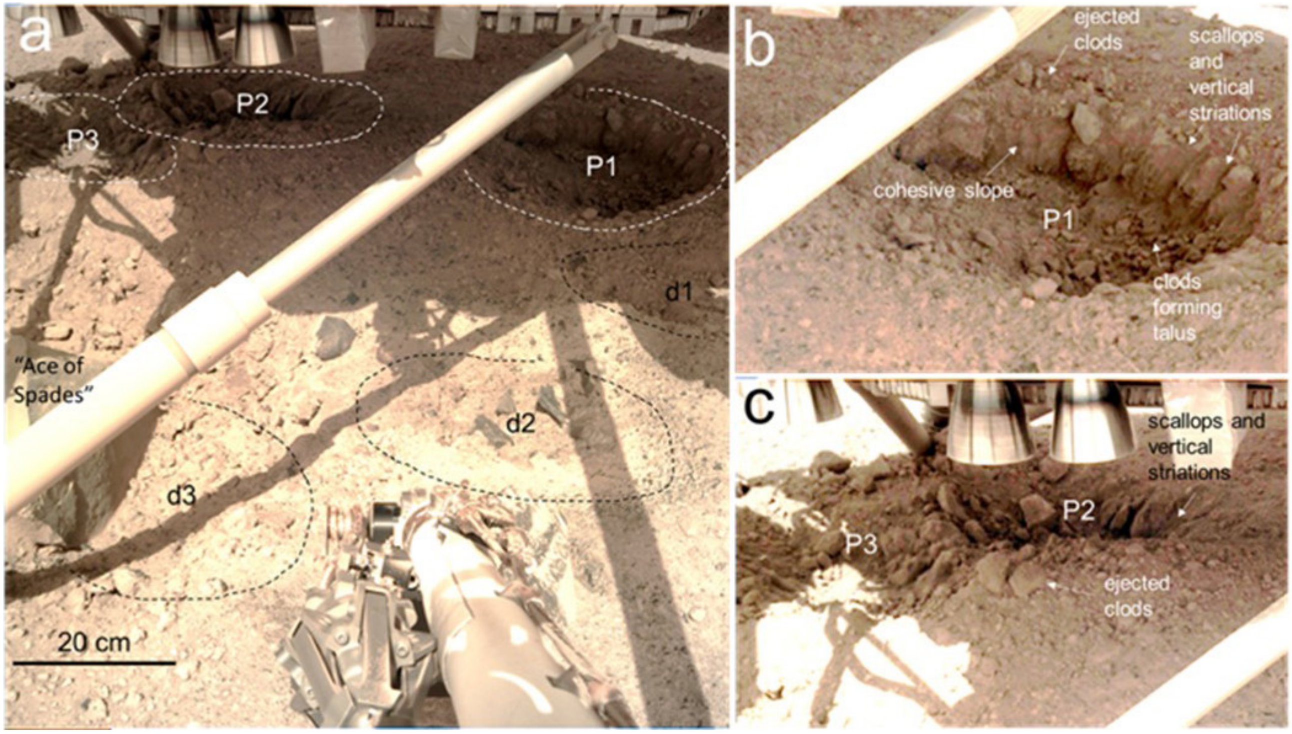

Figure 20. IDC images taken beneath the lander on sol 18. (a) The pits and depressions were excavated by the lander's retrorockets. P1 and P2 are the largest and deepest pits; (b) P1 is ~50 cm in diameter and reveals ~12 cm of the shallow stratigraphy; (c) View in more details of pits P2 and P3. The pit walls are vertically striated and steep (up to 65°) and expose an up to ~10 cm-thick cohesive duricrust comprised of cohesive fine sand. The floor of each pit contains abundant reddish, pebble-size clasts or clods of material that broke off the steep pit walls. Dark-grey pebbles of likely basaltic composition are visible within the matrix of fine sand (Warner et al., 2022).

temperature). Inversion of the thermal conductivity and diffusivity measurements would have allowed an estimate of the density as a function of depth, assuming the soil's heat capacity to be known. A mechanical strength profile for the soil would have been derived from the penetration rate that would have been recorded.

5.2.1 Mole penetration

Unfortunately, the mole did not penetrate deeper than ~37 cm at a final tilt of 30°, bringing the mole back-end 1-3cm below the surface. The record of the mole penetration attempts and related activities and inferences on the properties of the soil have been described in Spohn et al. (2022a). Lessons learned from the mole about penetrators have been discussed in Spohn et al. (2022b). Penetration attempts had started on sol 92 with 4000 hammer strokes. Instead of reaching the targeted mole tip depth of 70 cm, the tip was stuck at a then unknown depth (it was later determined that it had reached 32 cm depth). After a second attempt on sol 94 that brought no measurable progress and an intense campaign of diagnostics an almost two-year campaign of mole recovery was started on sol 308. Figure 21 shows a record of that period until the final penetration test on sol 754. Among the initial hypotheses for the mole's failure to penetrate were a) a stone blocking penetration and b) a lack of friction on the mole hull from the cohesive duricrust to balance recoil. The duricrust had already been observed in the pits excavated by the rocket exhaust below the lander (Figure 20). To provide additional friction, the mole was first pinned (pinning 1) using the scoop at the end of the Instrument Deployment Arm (Golombek et al., 2023). The techniques to help penetration are schematically shown below the graph. The schemes also indicate the 7 cm deep and 5-6 cm wide pit that had formed during the sol 92 and 94 hammering sessions by the mole precessing in the duricrust about a point midway along its hull.

The penetration attempts with pinning between sols 308 and 318 were successful bringing the mole 5 cm deeper in. This essentially disproved the conjecture of a stone blocking the way forward and supported the conjecture of a lack of friction from the duricrust. Because the mole was then too deep in for pinning to continue, it was tried to provide friction by pressing the scoop onto the surface next to the mole. The vertical stress would increase the overall stress around the mole and provide friction. This attempt failed and resulted in a reversal upward movement of around 28 cm (reversal 1) with an increase in tilt from 10° to 17°. The reversal was explained by sand filling in underneath the mole when it moved upwards during bouncing motions (the bouncing motions being the result of insufficient friction). The observation that the reversal motion ended when the mole tip was at a

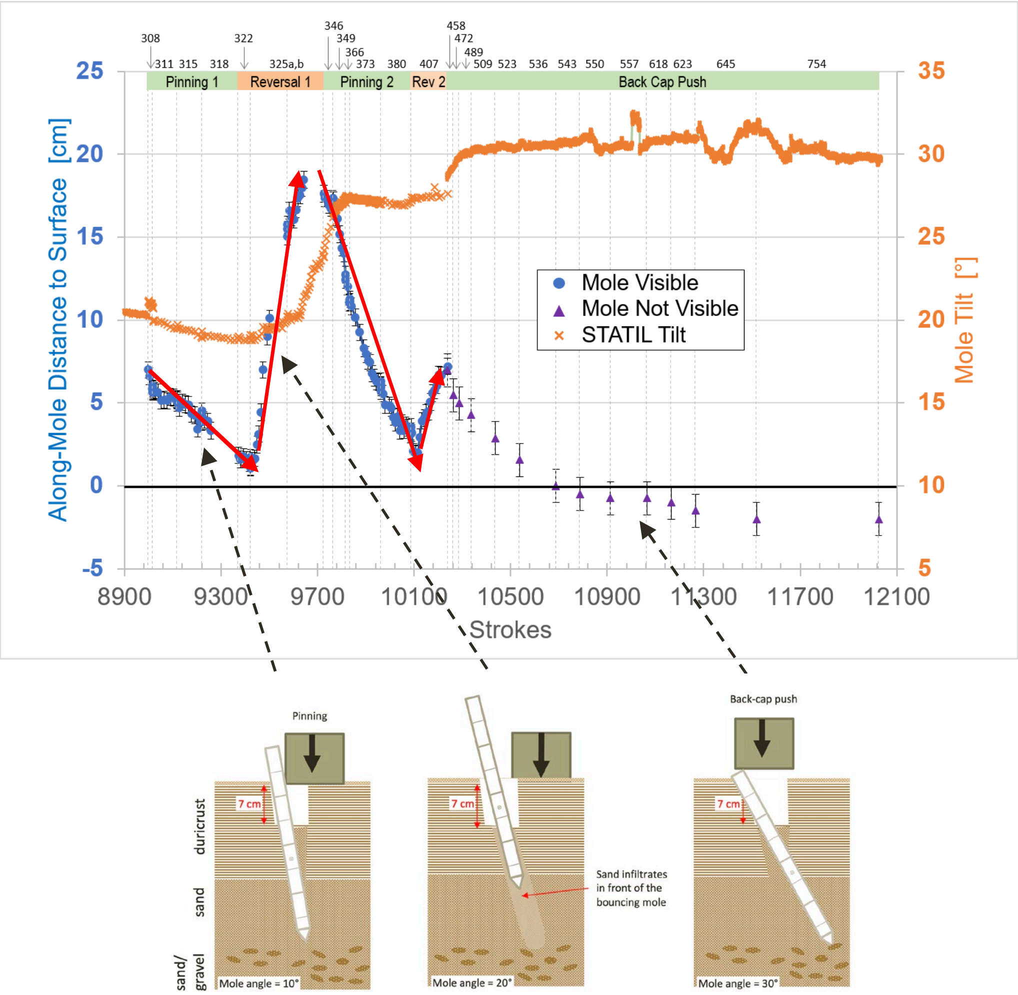

Figure 21. Mole penetration, strokes 8900 to 12100, described by the blue points in terms of distance between the back-end of the mole and the surface (given in cm in the left-hand vertical axis - 0 means that the mole is fully below the surface). The orange points give the mole inclination to vertical (right-hand vertical axis, in degrees). Individual sols when hammering occurred are indicated along the top border; vertical dashed lines show the boundaries of each sol's planned hammer strokes. The major periods of successful mole penetration (Pinning 1, Pinning 2, and Back Cap Push) are indicated by green horizontal bars along the top, while major periods of mole reversal (Reversal 1 and Reversal 2) are in orange (after Spohn et al., 2022a).

depth of about 20 cm was taken as indication that the mole had reached the bottom of the duricrust where sand was no longer available to freely fall in underneath the mole tip.

A second penetration (pinning 2), comparable to the first one was achieved at almost the same penetration degree, followed by a second reversal (rev. 2). Finally, it was decided to press the scoop directly on the top of the mole, achieving full penetration at sol 540 (with a final tilt of 30°).

Figure 22 presents an IDC photo of the "back cap push" session, in which the scoop of the IDA is compressing the regolith above the hole that developed during hammering, with the tether appearing on the left side of the scoop. The photo confirms the sand-like aspect of the surface regolith, with no rock in the area and some centimetre-sized pebbles around. Note also the perfectly smooth imprint of the scoop observed between the right side of the scoop and the elongated pile on the right. Such smooth surfaces have also been observed

Figure 22. IDC photo showing the scoop of the Instrument Deployment Arm pressing on the mole during the Back Cap Push session, with the tether on the left side. The scoop is 7.6 cm in width and 10 cm in length (image credit JPL/NASA).

on rover tracks in other missions and indicate that the fine particles contained in the sandy layer provide some degree of cohesion (Golombek et al., 2020a). A smooth surface was also observed during the indentation and pressing experiments carried out with the scoop, as shown in Figure 5 (see Section 5.3.2).

The mole was designed to penetrate cohesionless soil like quartz sand, which was initially expected to provide a good mechanical simulant material for Martian sand (see Section 4.2). The sand would provide friction to the buried mole hull to balance the remaining recoil of the mole hammer mechanism that drives the mole forward. Although a suppressor mass and spring in the hammer mechanism absorbed much of the recoil, the available mass did not allow a system that would have eliminated the recoil altogether (Spohn et al., 2022b). The root cause of the failure - as was determined through an extensive, almost two years long campaign (Spohn et al., 2022a, b) - was thus a lack of friction in an unexpectedly thick cohesive and brittle duricrust. In addition, it was found that the Martian soil provided unexpected levels of penetration resistance. A final "Free Mole Penetration" test in January 2021 to see whether the mole could continue penetrating without arm support failed, unfortunately, and the campaign was ended, also because of dwindling energy resources on the lander. The mole body remained 2-3 cm below the surface at which depth thermal conductivity measurements could be performed (Grott et al., 2021, 2023) for almost a Martian year.

5.2.2 Mechanical and thermal data derived from HP^3 measurements

The penetration record of the mole, the thermal conductivity and density measurements, the radiometer data and the seismic data recorded during the hammerings were used to derive a model of the properties of the first ~40 cm of the Martian soil at the landing site (Spohn et al., 2022a). Accordingly, as shown in the schemes of Figure 21, a duricrust of about 20 cm thickness is found underneath an about one-centimetre-thick unconsolidated sand and dust layer. Beneath the duricrust, a sand layer of about 10 cm thickness is found followed by a layer of a sand mixed with gravel, possibly consisting of debris from a small impact crater.

The penetration resistance of the sand/gravel layer is best constrained by the penetration data reported in Spohn et al. (2022a) and was found to be 5.3 MPa while the duricrust has a 5 to 10 times smaller penetration resistance. Compaction during the initial about 9000 strokes hammerings may have caused some densification of the lower layer. Applying cone penetration theory (e.g. Terzaghi & Peck, 1947; Poganski et al., 2017) the resistance of the duricrust was used to estimate a cohesion of the latter of 4-25 kPa, depending on the assumed internal friction angle of the duricrust. Pushing the scoop with its blade into the surface and chopping off a piece of duricrust provided another estimate of the cohesion of about 6 kPa.

There are no direct measurements of soil density at the InSight landing site, but inversion of the thermal conductivity measurements performed by the HP^3 TEM-A (Thermal Excitation and Measurement-Active mode, Grott et al., 2021) after the mole was fully buried allows an estimate of the average density of the top 40 cm of the soil of 1211^{+149}_{-113} kg/m^3.

The average thermal conductivity was found to be 0.039 ± 2 W/m K (Grott et al., 2021). Based on the scheme of Figure 21, Spohn et al. (2022a) suggest that the thermal conductivity increases from 0.014 W/m K to 0.034 W/m K through the one-centimetre thick surface sand/dust layer, keeps the latter value in the duricrust and the sand layer underneath and then increases to 0.064 W/m K in the sand/gravel layer below. The density is 1300 kg/m^3 in the sand/dust layer, 950-1100 kg/m^3 in the duricrust, 1300-1500 kg/m^3 in the sand layer and 1600 kg/m^3 in the sand/gravel layer beyond 31 cm depth. These values are in good agreement with the thermal inertias at the InSight landing site, that correspond to thermal conductivities $k = 0.041 \pm 0.013$ mW m^{-1} K^{-1}. Due to low atmospheric pressure and gravity typical of Mars, these are very low values compared to those of current terrestrial soils, where k is close to 1 W m^{-1} K^{-1}.

Grott et al. (2023) have studied the variation of the thermal conductivity through the Martian seasons (solar longitude between 8° and 210°) and with the atmosphere pressure. They found that the thermal conductivity varied by ±5%; the error of the measurements being ±2.6%. Their results confirm that atmosphere gas contributes in a major way to the heat transfer in the regolith, as experimentally demonstrated by Nagihara et al. (2022). For cohesionless and non-cemented soils, the measured thermal conductivity values indicate that 85-95% of all particles are smaller than 104-173 μm (Presley & Christensen, 1997; Grott et al., 2021; Piqueux et al., 2021).

Further observation of the near-surface has been made possible by the pit that developed around the mole during hammering, observable once the support structure was removed by the IDA.

The photo of Figure 23 shows the pit created around the inclined mole (inclined 15°), with an almost vertical wall made up of resistant layers containing some pebbles. The steep edge and some overhangs indicate the existence of cohesion. Pebbles are embedded in a fine-grained matrix, indicating cementation. The resulting cohesion is at the origin of the lack of friction that jeopardized the mole penetration.

5.2.3 Pressing experiments on the mole pit

The shear strength parameters of the regolith were determined by analysing experiments conducted with the robotic arm between sols 240 and 250 (Spohn et al., 2022a; Golombek et al., 2023; Marteau et al., 2021, 2022, 2023). In these experiments, pressure was applied on the ground using the robotic arm's scoop near the open pit that formed

Figure 23. Image of the pit (7 cm deep, 5-6 cm wide) created by the HP3 mole during hammering (inclined ~15°), with the scoop appearing on top right (image credit JPL/NASA).

Figure 24. IDC photo showing the scoop of the IDA compressing the regolith with the mole (not in contact with the scoop, with the tether clearly visible) moved up during a reversal period (see Figure 20). The mole pit can be observed at the left of the scoop (image credit JPL/NASA).

around the HP^3 mole during initial hammering, as showcased in Figure 24.

The scoop can be positioned to exert pressure on the ground either with its flat surface (Figure 24) or with its tip. A three-dimensional slope stability analysis was conducted, considering an elasto-plastic Mohr-Coulomb failure criterion as the soil's material model. The soil unit weight in the Martian environment was set at 4.52 kN/m^3, which corresponds to a unit mass of 1220 kg/m^3 under the gravity of Mars (3.721 m/s^2). A friction angle $\phi' = 30°$ was fixed for all calculations, and the cohesion required to fulfil the stability criteria with a safety factor of 1 was determined iteratively. The dimensions of the HP^3 mole pit, as determined by the images acquired by the arm-mounted camera, are 0.045 m in width and 0.07 m in height. The slope inclination of the pit was measured at 85°, indicating a steep slope. The force exerted by the scoop on the ground was estimated based on an algorithm, that takes into account the joint position of the arm as well as the current and torque measurements from the actuators on Mars. However, it should be noted that the acquisition rate of these measurements is low and that they may be subjected to noise, potentially leading to inaccuracies in the force measurements. The force exerted during the flat push was measured to be 29 N, resulting in a pressure of 7.9 kPa, whereas the force measured during the tip push was 45 N, corresponding to a distributed load of 91.9 kPa. The inferred minimum cohesion values for the flat push and tip push were found to be c' = 0.4 kPa and 5.8 kPa, respectively (Marteau et al., 2021, 2022, 2023).

5.3 In-situ determination of elastic properties

The elastic properties of the regolith have an important influence on the seismic wavefield and travel times as recorded by the SEIS instrument. A specific example is site effects, i.e., the influence of shallow near-receiver structure on seismic recordings, which are well known in terrestrial seismology. Knowledge of the elastic properties of the regolith will help to better understand these effects which will need to be considered when analysing signals in the affected frequency range.

5.3.1 Local wave velocity measurements

The seismometer SEIS was placed at a distance of around 1.227 m from the HP^3 self-hammering mole (Figure 25, see also Figure 3 and Figure 5, Golombek et al., 2020b). At some point during the mission preparation, it was realised that recording the mole hammering signals offered a unique opportunity to study the elastic properties at the landing site, comparable, in terrestrial geotechnics, to some kind of cross-hole test. However, because SEIS was designed to record mars quakes and a direct link between the HP^3, SEIS and lander clocks was not established, a series of adaptations had to be implemented. During hammering of the HP^3 mole, SEIS was set to a specific mode to enable recording the seismic hammering signals in high temporal resolution beyond the nominal sampling frequency of 100 Hz. Furthermore, an adapted time keeping a clock correlation scheme was implemented to estimate the travel times and, hence, the seismic velocity of the regolith volume between the HP^3 mole and SEIS (Kedar et al., 2017; Sollberger et al., 2021; Brinkman et al., 2022).

Brinkman et al. (2022) processed the SEIS waveform recordings of around 2000 hammer strokes (Figure 26). The three-component seismic data were rotated to separate the *P*- and *S*-wave components of the wavefield such that

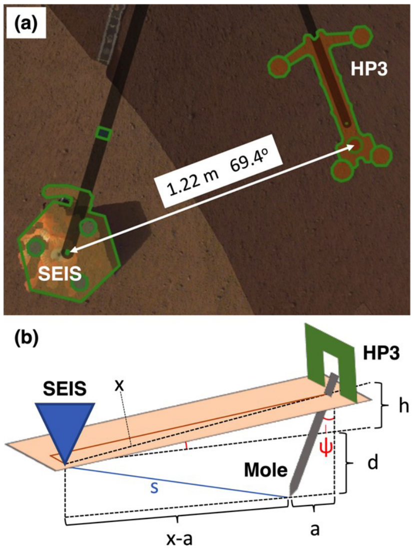

Figure 25. (a) Graphical representation of SEIS and HP^3; (b) Schematic illustration of the SEIS, HP^3 and mole geometry. SEIS and HP^3 are separated by a distance x = 1.227 m. The 40 cm-long mole is inclined by an angle $\psi \approx 30°$ (see Figure 20). Figure modified from Brinkman et al. (2022).

travel times for both the *P*- and *S*-wave first arrivals could be picked manually for 2271 hammer stroke recordings. The location of the mole tip, which was assumed to have acted as seismic source when hammering, was reconstructed from images taken by the two cameras (Figure 25). The distance *s* between the tip of the 40 cm-long mole and the centre of SEIS could be determined for 1518 hammer strokes, and varied between 1.08 m and 1.17 m depending on the (varying) inclination ψ of the mole (Figure 26b).

Given the manually picked travel times and the distance *s* between the mole tip and SEIS, apparent seismic velocities were computed obtaining velocity values $V_p = 119^{+45}_{-21}$ m/s and $V_s = 63^{+11}_{-7}$ m/s, respectively (Figure 27). The estimates follow log-normal distributions with given mode and 68.3% confidence interval values. Because the *P*- and *S*-wave travel times show a similar scatter in terms of magnitude, the relative error of V_p is larger than the relative error of V_s. A complementary study of the apparent incidence angle of 2'461 *P*-wave first arrivals revealed an independent V_p/V_s ratio estimate of $1.84^{+0.89}_{-0.35}$, which is in good agreement with the travel time-derived value of $1.86^{+0.42}_{-0.25}$. These velocity estimates likely reflect properties of the bulk volume of the uppermost 10s of cm of the regolith layer.

Because SEIS was located only around one seismic wavelength away from the source, Brinkman et al. (2022) addressed concerns that near-field effects could affect their analyses and confirmed their results with an extensive numerical full-wavefield simulation study.

Assuming a density of 1200 kg/m^3 (see above), we can convert the V_p and V_s estimates by Brinkman et al. (2022) into a bulk, shear, and Young's modulus of 9.8 ± 6.8 MPa, 4.3 ± 1.0 MPa, 11.3 ± 2.9 MPa, respectively, and a Poisson's ratio ν of 0.31 ± 0.15. When interpreting these numbers, one has to keep in mind that they are effective values of a homogeneous half-space and resulted from seismic observations with a dominant frequency of around 60 Hz.

Comparisons of the prelanding predicted low seismic regolith velocities on Mars with terrestrial soil and planetary regolith studies have extensively been discussed in Morgan et al. (2018). Similar low P-wave velocities of 100-120 m/s have been observed during laboratory tests with different Martian regolith simulants and low overburden pressure (Delage et al., 2017, see also Figure 14). For the Moon, active source (e.g. Cooper et al., 1974) and passive (e.g. Sens-Schönfelder & Larose, 2010) seismic experiments from Apollo 14, 16, and 17 as well as laboratory studies on lunar regolith samples (Johnson et al., 1982) found P-wave velocities in the range of around 100-125 m/s at, or close to, the surface. Published lunar S-wave velocities at the surface range between around 30 and 60 m/s (e.g. Dal Moro, 2015; Larose et al., 2005; Tanimoto et al., 2008), and reported Poisson's ratios range between 0.23 and 0.43 (e.g. Larose et al., 2005). Interestingly, these Poisson's ratios are generally higher than the predicted value for the InSight landing site that was estimated prelanding (i.e. 0.22 by Delage et al., 2017) but agree reasonably well with the Poisson's ratio of 0.28 found in this study. The elastic parameter estimates are also in general agreement with values derived with other approaches, e.g., SEIS/soil interaction on sandy simulants (Fayon et al., 2018; Delage et al., 2022), analysis of SEIS and lander resonances (e.g. Lognonné et al., 2020; Stott et al., 2021) and HP^3 mole recovery activities (Spohn et al., 2022a).

5.3.2 Elastic properties experiments

Some experiments to measure the elastic properties of the Martian regolith by pressing on the Martian ground using the scoop on the robotic arm were carried out (Golombek et al., 2023). This can be observed in the photo of Figure 5, where the scoop is pressing the soil on the right-hand side of SEIS. One can also observe in the photo an imprint of a former press tests.

Pressing the soil with the scoop causes the ground to incline slightly towards the scoop, generating a tilt of SEIS that is observable on the horizontal component of the seismometer. Assuming that the inclination angle (θ) is very small, the acceleration due to the local ground tilt can be approximated as $g\theta$, where g is the local gravitational acceleration ($g = 3.721$ m/s^{-2}). A quasi-static elastic surface deformation approach (as described in Murdoch et al., 2017a, b) can then be used to invert θ in order to retrieve the mean elastic parameters of the ground between the scoop and SEIS.

These experiments require some measurements of the vertical (F_v) and radial (F_r) force components, that are derived from the electric intensity in the IDA motors during the test. This was made through calibration tests carried out in the JPL testbed.

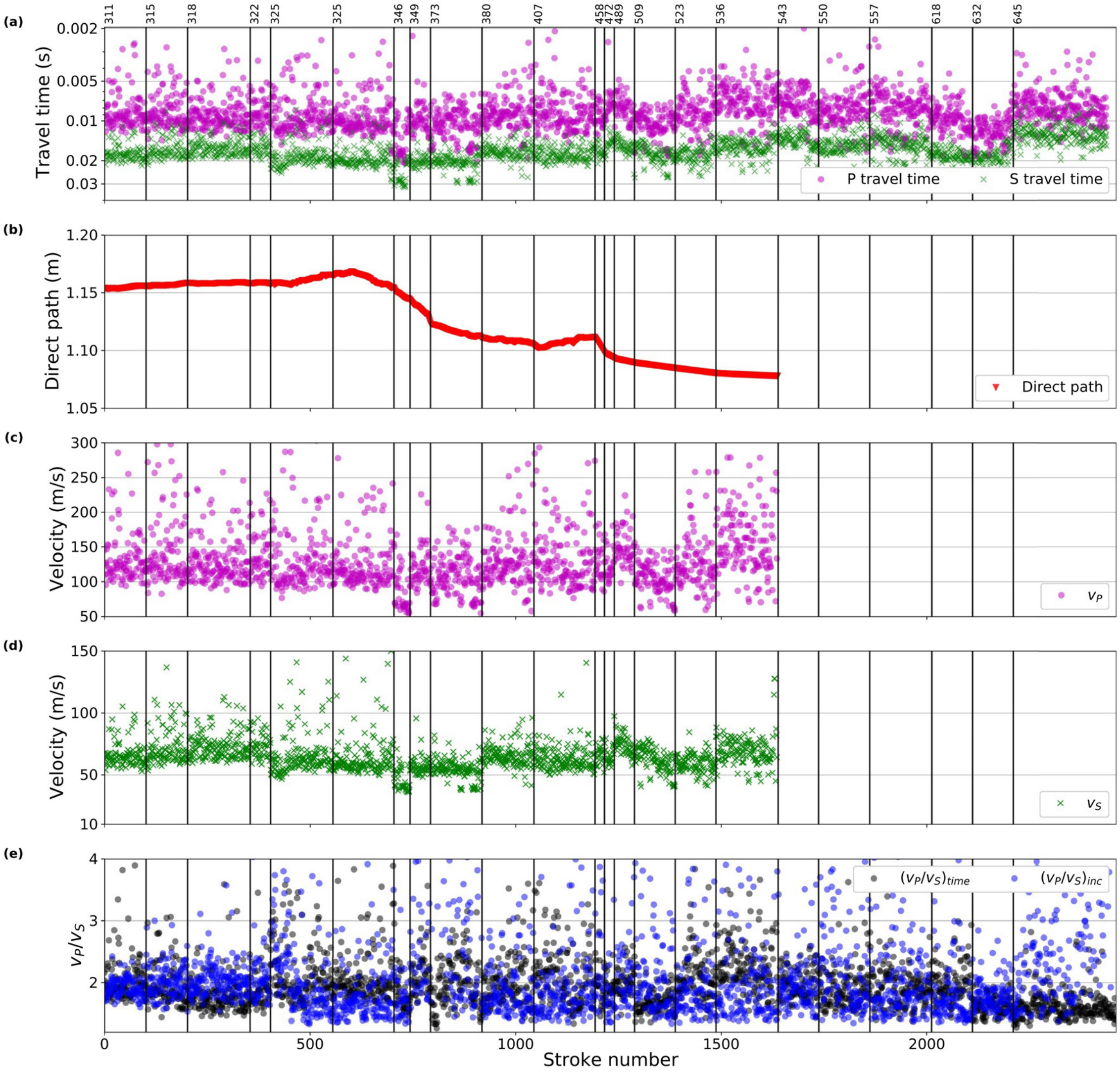

Figure 26. (a) First-arrival P- (t_P) and S-wave (t_S) travel time picks for the hammer sessions conducted between sols 311 and 645; (b) Distance between the HP^3 mole tip and the SEIS seismometer; (c) Effective *P*- (V_P) and (d) *S*-wave velocity (V_S) estimates based on the travel times and travel path distances shown in (a) and (b), respectively; (e) $(V_P / V_S)_{\text{time}}$ ratio estimates derived from t_S/t_P using the travel time data displayed in panels (a) and (b) plotted together with the incidence angle-derived $(V_P / V_S)_{\text{inc}}$ (Brinkman et al., 2022).

The first scoop pressing experiment, performed on sol 1156, involved pressing on the ground with a (near) vertical force. This was to ensure that the tilt signal on SEIS was detectable, to reduce the error in the knowledge of the force applied by the scoop, and because this allowed the elastic properties experiment to be combined with an indentation experiment that required vertical forcing. The location selected to implement this experiment (see Figure 5) was chosen to be suitable for both the indentation and elastic properties experiments, and feasible for the IDA team. A second scoop pressing experiment was performed on sol 1170, with a larger radial force component (F_r), in order to further constrain ground properties. With only vertical forcing (F_v) it is possible, in principle, to constrain the relationship between elastic parameters, but adding radial forcing allows to simultaneously resolve all the elastic ground parameters. The location of the second elastic properties experiment, about 48 cm outboard from the first experiment (see Figure 5), was selected such that F_r/F_v was about 0.93, based on calibrations done in the InSight JPL testbed. These data are still being analysed, but initial results suggest Poisson's ratio is around 0.25 and the shear modulus is around 2 MPa, which are comparable to those derived from SEIS recordings of hammering experiments (Brinkman et al., 2022). Note however that further investigations have to be conducted to account in more details, in the comparison of the elastic parameters obtained, for the morphology of the surface layers given in Spohn et al. (2022a) and further commented in Section 6.

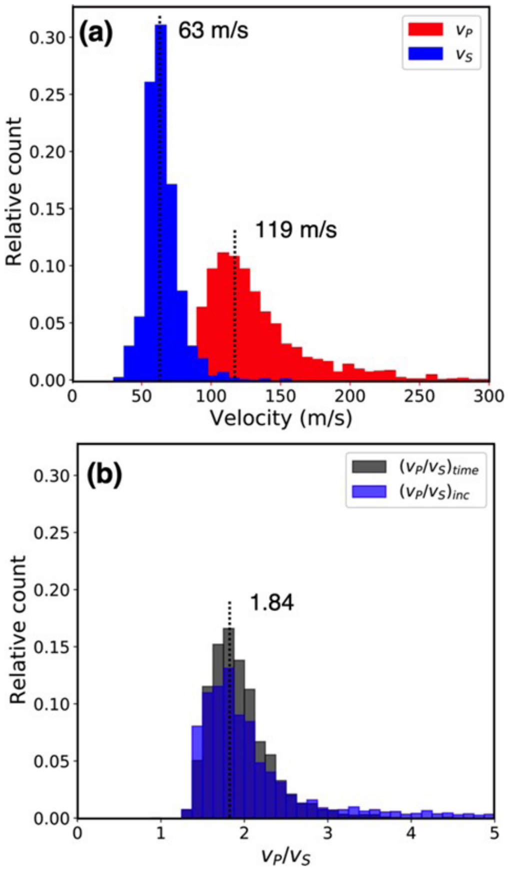

Figure 27. (a) Histogram of 1 518 P- (V_p) and S-wave (V_s) velocity estimates; (b) Histogram of 2 271 $(V_p / V_s)_{time}$ values determined from the picked travel times and 2 461 $(V_p/V_s)_{inc}$ values determined from the *P*-wave incidence angles. The dashed lines mark the mode of each distribution. Figure modified from Brinkman et al. (2022).

5.4 Scraping and dumping activities

The robotic arm and scoop were also utilised to bury the SEIS tether so as to reduce the perturbations due to the change in temperature of the tether and to its interactions with the wind. This was made by creating numerous scrapes, scooping regolith, and dumping it. Several scraped piles were created from which regolith was collected using the scoop, (Golombek et al., 2023) as shown in Figure 5 and in more details in Figure 28.

The regolith extracted in the scoop was then dumped in piles above the tether, close to the SEIS instrument. However, some of the regolith was observed to be blown away by the wind, as reported by Golombek et al. (2023) and Verdier et al. (2023). This constrained the grain size distribution curve of the poured regolith by integrating the combined effects of wind and gravity on the poured grains.

To assess the topography of the scraped and dumped piles, digital elevation models and elevation profiles were generated from the images acquired between Sols 803 and 822. Figure 29 provides an example of the digital elevation model and elevation profiles obtained on Sol 822. The average slope of the scraped mounds was found to be approximately 42° (with a standard deviation of 2.7°) (Marteau et al., 2022, 2023), while the slopes of the side walls created by the vertical sides of the scoop were steeper, with a slope value of 54.7° (with a standard deviation of 6.6°). These values are significantly larger than what could be derived from the friction angle of the sandy regolith, estimated to be around 30° in the loose state met at the surface (Delage et al., 2017; Morgan et al., 2018). Note however that the slopes along P1 and P2 in Figure 29 are not those of a standard pile, put of a regolith mass either pushed and remoulded by the scoop (P1), or slopes of the walls on both sides of a trench. This certainly deserves further investigation, but it seems that the particular conditions prevailing on Mars (low gravity, low atmospheric pressure) together with the presence of dust within the sandy regolith result in having some cohesion that allow steeper slopes than that corresponding to the angle of repose. It is worth noting that the cohesion is further enhanced by the low gravity conditions on Mars, as observed on lunar regolith by Walton et al. (2007).

Subsequently, the IDA scooped up the scraped material and dumped it from a height of 40 cm on top of the SEIS tether. The highest point of the dumped pile reaches a height of approximately 3 cm, with a slope value of 24.1° (with a standard deviation of 6.1°). Note that, as calculated by Verdier et al. (2023), the grain size distribution of the poured regolith is different from that of the scraped one, since the smaller particles (200 µm and below) have been blown by the wind and deposited in plumes at distances up to 3-5 m from the scoop, whereas the particles smaller than 100 µm and below (including dust) are blown away. This can be observed in the photo of Figure 30 (Verdier et al., 2023) that shows the situation before (a) and after (b) a dump. The plume of deposited finer particles observed as a dark elongated spot in (c) has been obtained by differencing the images (a) and (b).

The smaller slope of 24.1° of the dumped pile (Marteau et al., 2023) is satisfactorily in agreement with the estimated 30° angle of friction of the loose regolith. This smaller friction value for the regolith without its finest and dust fraction is in agreement with the cohesion that is suspected to be provided by the dust fraction (< 10 µm) in the intact regolith, that no longer exist in the poured regolith due to the wind dispersion of smallest particles.

6. A model of the soil profile at the InSight landing site

The diagram of Figure 31, based on visual observations of the photos (Figures 3, 5, 20, 22, and 23) and on data from both the mole penetration process (Spohn et al., 2022a) and local wave velocity measurements (Brinkman et al., 2022) provide a synthesis of the estimated physical and mechanical properties of the near surface. Below a 1 cm thick surface dust/sand deposit, an around 19 cm thick duricrust layer rests

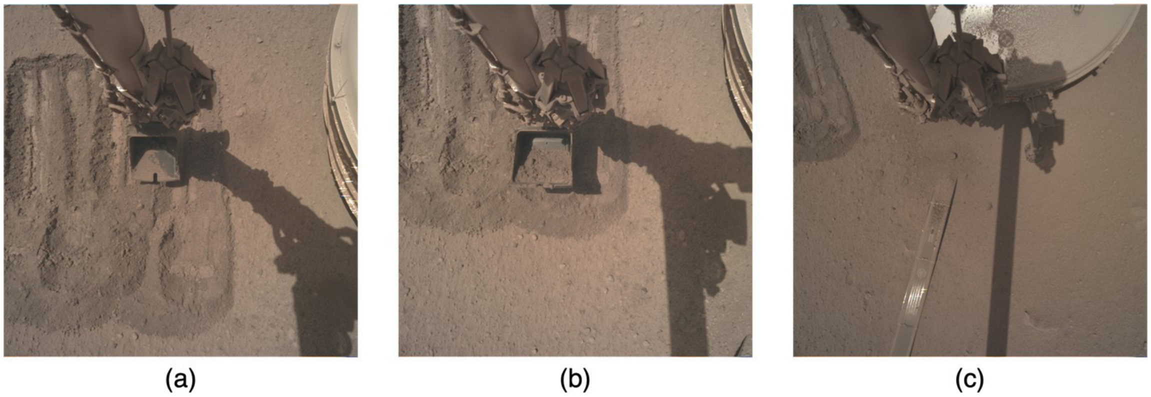

Figure 28. Photos acquired on sol 870: (a) Scraped piles; (b) Scooped regolith; (c) Regolith dumped on the SEIS tether close to the WTS (Image credit NASA/JPL).

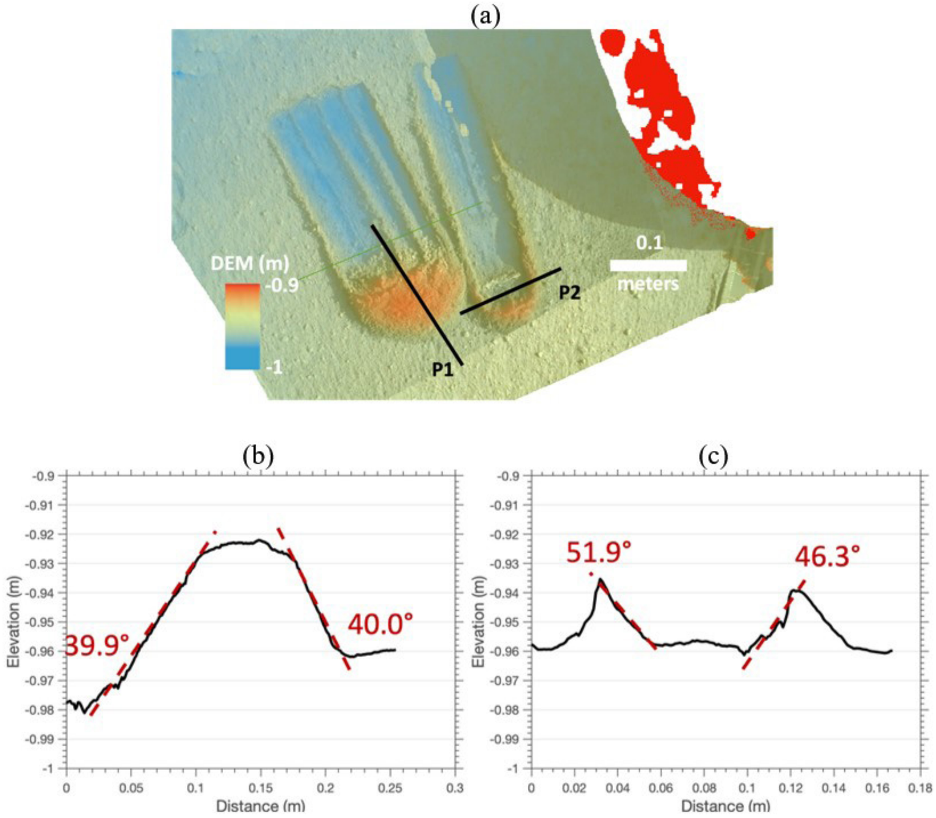

Figure 29. (a) Sol 822 Digital Elevation Model; (b) Elevation profile of scraped pile P1; (c) Elevation profile of scraped walls P2.

on an around 12 cm thick sand layer overlaying a sand/gravel layer of unknown thickness beginning at a depth of 31 cm. The Figure also shows that the elastic properties derived from the HP^3/SEIS measurements are representative of the averaged elastic properties of the of the sand and duricrust layer, with densities of 1300-1500 kg/m^3 and 950-1100 kg/m^3, respectively. It is important to also remind that waves travel in surface under quite low stresses, given the smaller gravity on Mars. With $g = 3.721$ m/s^{-2}, for the profile of the Figure, the vertical stress σ_v is equal to around 1.35 Pa at 31 cm depth where the waves are emitted by hammering and reduce to 0.045 Pa at 1 cm depth. Present knowledge on wave transfer in granular (and/or slightly cohesive) materials under such very low stresses is presently not well known and certainly deserves further investigation, with particular attention to the effect of particle shape and rugosity at inter-grains contacts.

Consistent with the formation process of the regolith (see Figure 7) and from observing the photos taken around the InSight landing site by the two cameras, Golombek et al. (2020a) proposed the sketch of Figure 32 to describe the

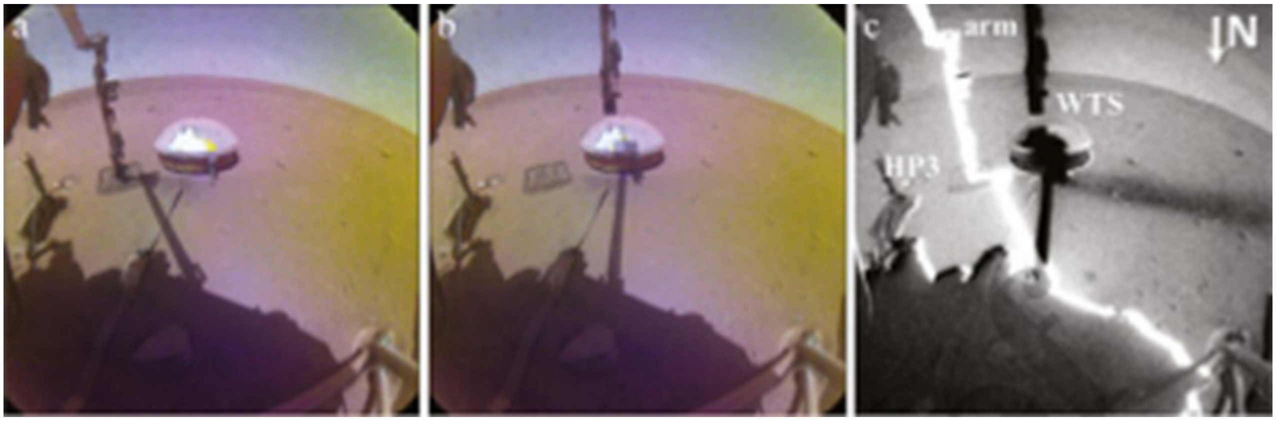

Figure 30. (a) Instrument Context Camera (ICC) image taken on sol 877 at 11:22 a.m. before dump 6 on the SEIS tether; (b) ICC image acquired on sol 877 at 11:33 a.m., after dump 6; (c) ICC image difference showing the dark plume made up of wind dispersed and transported particles. The plume extends to the right from the WTS, and its orientation corresponds to the wind direction from N14° (ESE) to N320° (WNW) (Verdier et al., 2023).

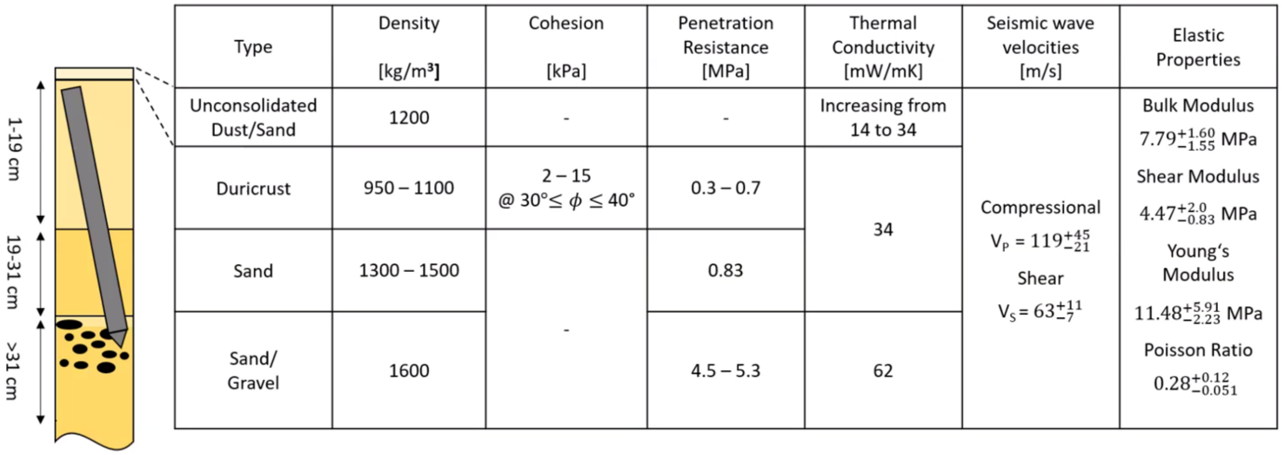

Type	Density [kg/m³]	Cohesion [kPa]	Penetration Resistance [MPa]	Thermal Conductivity [mW/mK]	Seismic wave velocities [m/s]	Elastic Properties
Unconsolidated Dust/Sand	1200	-	-	Increasing from 14 to 34	Compressional $V_P = 119^{+45}_{-21}$ Shear $V_S = 63^{+11}_{-7}$	Bulk Modulus $7.79^{+1.60}_{-1.55}$ MPa Shear Modulus $4.47^{+2.0}_{-0.83}$ MPa Young's Modulus $11.48^{+5.91}_{-2.23}$ MPa Poisson Ratio $0.28^{+0.12}_{-0.051}$
Duricrust	950 – 1100	2 – 15 @ $30° \leq \phi \leq 40°$	0.3 – 0.7	34		
Sand	1300 – 1500	-	0.83			
Sand/ Gravel	1600		4.5 – 5.3	62		

Figure 31. Estimated properties of the near surface (Spohn et al., 2022a). Thermal properties are from Grott et al. (2021); Seismic wave velocities and elastic properties are from Brinkman et al. (2022), see Section 5.3.1.

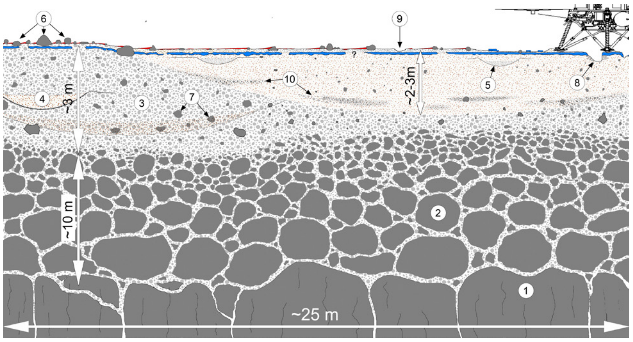

Figure 32. Interpretative cross-section of the shallow surface beneath the InSight lander. (1) Fractured basalt flow; (2) Blocky ejecta; (3) Fine-grained impact generated regolith; (4, 5) Overlapping craters; (6) Rockier area; (7) Rocks embedded in regolith; (8) Pits opened by retro rockets during landing; (9) Surface divots; (10) Lens of ejecta from other craters. (Golombek et al., 2020a).

structure of the regolith along a deeper profile in the landing area. A depression of ~27 m in diameter (in which the lander sits) interpreted as an ancient degraded and infilled impact crater in the regolith is underlain by blocky ejecta and fractured basaltic bedrock. The crater has been filled dominantly by sand moved by the wind, producing an upper layer of fine material three metres thick, consisting mostly of sand.

7. Conclusion

The InSight mission was quite successful on a geophysical point of view, but the various instruments accommodated by the InSight lander also provided significant input on the geological and geotechnical properties of the near surface. This concerns the high-quality photos provided by the cameras, the data from the self-penetrating mole, the wave recordings by the SEIS seismometer and all the activities carried out with the Instrument Deployment Arm and its scoop. In spite of the significant difference in nature between the true soil profile and the sandy regolith simulants considered in the pre-mission investigations, a rather good agreement was found for the elastic properties at surface, derived from wave velocity measurements. These were well characterised by conducting some kind of Martian cross-hole test, by analysing with SEIS the waves resulting from the mole hammering sessions. The penetration phases of the self-penetrating mole, in spite of being problematic, provided a significant input on the soil profile along the first 30 cm penetrated, completed by the photos taken from the IDC camera located on the IDA. The profile initially observed under the lander in the area affected by the impingement of the rocket exhaust was confirmed by observing the pit around the mole and analysing the penetration data. Other significant information was given by the scraping, piling and pushing activities carried out by the Instrument Deployment Arm to help the mole penetration and to cover the SEIS tether to improve its thermal and mechanical insulations. The surface regolith, suspected to be sandy with an average grain diameter of 170 µm from orbiter thermal inertia measurements and surface radiometer measurements, appeared to have a profile in which a 1 cm sand/dust layer is overlaying a layer made up of a loose cohesive matrix with embedded pebbles, called duricrust. Below, as derived from penetration data, the profile includes a sandy layer covering a gravel/sand layer in which the mole penetration was stopped.

The scrapping operations only concerned the 1 cm thick surface sand/dust layer, given that the scoop was not able to excavate deeper into the underlain cohesive duricrust. The Digital Elevation Models provided more details on the excavated trenches and poured piles, with angles of slopes that were sometimes significantly larger than the angle of repose and friction angle (estimated around 30° for the loose surface sandy deposit). The steep slopes observed in trenches are suspected to be due to some cohesion resulting from the presence of dust and some bonding agents in the surface layer, and from the effects of low gravity. Interestingly, the slope of the piles of poured regolith, in which no dust and fine particles remained due to the action of the wind, were close to the estimated angle of friction.

The observations and measurements made with the various InSight instruments definitely enriched the knowledge of the geological and mechanical properties of the surface regolith and will certainly help for further robotic exploration of the surface of Mars.

Acknowledgements

We acknowledge NASA, CNES, their partner agencies and Institutions (UKSA, SSO, DLR, JPL, IPGP-CNRS, ETHZ, IC, MPS-MPG) together with Ecole des Ponts ParisTech (France) and Universidad de los Andes (Colombia) for supporting this work. Part of this research was carried out at the Jet Propulsion Laboratory, California Institute of Technology, under a contract with the National Aeronautics and Space Administration (80NM0018D0004). This paper is InSight Contribution Number ICN 272.

Declaration of interest

The authors have no conflicts of interest to declare. All co-authors have observed and affirmed the contents of the paper and there is no financial interest to report.

Authors' contributions

Pierre Delage: supervision, conceptualization, writing – original draft, review and editing. Bernardo Caicedo: conceptualization, writing – original draft. Matt Golombek: formal analysis, data analysis, conceptualization, writing – original draft. Tilman Spohn: funding acquisition, project administration, data analysis, writing – original draft. Cédric Schmelzbach: investigation, data curation, writing – original draft. Nienke Brinkman: investigation, data curation, formal analysis. Eloise Marteau: investigation, data curation, formal analysis, writing – original draft. Naomi Murdoch: investigation, data curation, formal analysis, writing – original draft. Nicholas Warner: investigation, data curation, formal analysis, conceptualisation. Véronique Ansan: investigation, data curation, formal analysis, conceptualisation, visualisation. Bruce Banerdt: funding acquisition, project administration, conceptualisation. Juan-Pablo Castillo-Betancourt: data curation, formal analysis, visualisation. Pascal Edme: data curation, formal analysis. Annabel Gomez: investigation, data curation, formal analysis. Matthias Grott: investigation, data curation, formal analysis, writing – original draft. Ken Hurst: investigation, data curation, formal analysis, methodology. Mark Lemmon: data curation, formal analysis. Philippe Lognonné: funding acquisition, project administration, conceptualisation. Sylvain Piqueux: investigation, data curation, formal analysis, methodology. Johann Robertsson: data curation, formal analysis, conceptualisation, methodology. David Sollberger: data curation, formal analysis, conceptualisation, visualisation, methodology. Simon Stähler: data curation, formal analysis, conceptualisation. Nicolas Verdier: data curation, formal analysis, conceptualisation. Christos Vrettos: data curation, formal analysis, conceptualisation. Nathan Williams: data curation, formal analysis, conceptualisation.

Data availability

No dataset was generated or evaluated in the course of the current study; therefore, data sharing is not applicable.

References

Andria-Ntoanina, I. (2011). *Caractérisation dynamique de sables de référence en laboratoire: application à la réponse sismique de massifs sableux en centrifugeuse* [Doctoral thesis]. École des Ponts ParisTech, Université Paris-Est (in French).

Arvidson, R.E., Ruff, S.W., Morris, R.V., Ming, D.W., Crumpler, L.S., Yen, A.S., Squyres, S.W., Sullivan, R.J., Bell III, J.F., Cabrol, N.A., Clark, B.C., Farrand, W.H., Gellert, R., Greenberger, R., Grant, J.A., Guinness, E.A., Herkenhoff, K.E., Hurowitz, J.A., Johnson, J.R., Klingelhöfer, G., Lewis, K.W., Li, R., McCoy, T.J., Moersch, J., McSween, H.Y., Murchie, S.L., Schmidt, M., Schröder, C., Wang, A., Wiseman, S., Madsen, M.B., Goetz, W., & McLennan, S.M. (2008). Spirit Mars Rover Mission to the Columbia Hills, Gusev crater: mission overview and selected results from the Cumberland Ridge to Home Plate. *Journal of Geophysical Research*, 113(E12), E12S33. http://dx.doi.org/10.1029/2008JE003183.

Arvidson, R.E., Bonitz, R.G., Robinson, M.L., Carsten, J.L., Volpe, R.A., Trebi-Ollennu, A., Mellon, M.T., Chu, P.C., Davis, K.R., Wilson, J.J., Shaw, A.S., Greenberger, R.N., Siebach, K.L., Stein, T.C., Cull, S.C., Goetz, W., Morris, R.V., Ming, D.W., Keller, H.U., Lemmon, M.T., Sizemore, H.G., & Mehta, M. (2009). Results from the Mars Phoenix Lander Robotic Arm experiment. *Journal of Geophysical Research*, 114(E1), e2009JE003408. http://dx.doi.org/10.1029/2009JE003408.

Bachrach, R., Dvorkin, J., & Nur, A.M. (2000). Seismic velocities and Poisson's ratio of shallow unconsolidated sands. *Geophysics*, 65(2), 559-564. http://dx.doi.org/10.1190/1.1444751.

Bahrami, M., Yovanovich, M.M., & Culham, J.R. (2005). A compact model for spherical rough contacts. *Journal of Tribology*, 127(4), 884-889. http://dx.doi.org/10.1115/1.2000982.

Baker, M., Newman, C., Charalambous, C., Golombek, M., Spiga, A., Banfield, D., Lemmon, M., Banks, M., Lorenz, R., Garvin, J., Grant, J., Lewis, K., Ansan, V., Warner, N., Weitz, C., Wilson, S., & Rodriguez, S. (2021). Vortex-dominated aeolian activity at InSight's landing site, part 2: local meteorology, transport dynamics, and model analysis. *Journal of Physical Research. Planets*, 126(4), e2020JE006514. http://dx.doi.org/10.1029/2020JE006514.

Banerdt, W.B., Smrekar, S.E., Banfield, D., Giardini, D., Golombek, M., Johnson, C.L., Lognonné, P., Spiga, A., Spohn, T., Perrin, C., Stähler, S.C., Antonangeli, D., Asmar, S., Beghein, C., Bowles, N., Bozdag, E., Chi, P., Christensen, U., Clinton, J., Collins, G.S., Daubar, I., Dehant, V., Drilleau, M., Fillingim, M., Folkner, W., Garcia, R.F., Garvin, J., Grant, J., Grott, M., Grygorczuk, J., Hudson, T., Irving, J.C.E., Kargl, G., Kawamura, T., Kedar, S., King, S., Knapmeyer-Endrun, B., Knapmeyer, M., Lemmon, M., Lorenz, R., Maki, J.N., Margerin, L., McLennan, S.M., Michaut, C., Mimoun, D., Mittelholz, A., Mocquet, A., Morgan, P., Mueller, N.T., Murdoch, N., Nagihara, S., Newman, C., Nimmo, F., Panning, M., Pike, W.T., Plesa, A.-C., Rodriguez, S., Rodriguez-Manfredi, J.A., Russell, C.T., Schmerr, N., Siegler, M., Stanley, S., Stutzmann, E., Teanby, N., Tromp, J., van Driel, M., Warner, N., Weber, R., & Wieczorek, M. (2020). Initial results from the InSight mission on Mars. *Nature Geoscience*, 13(3), 183-189. http://dx.doi.org/10.1038/s41561-020-0544-y.

Banfield, D., Rodriguez-Manfredi, J.A., Russell, C.T., Rowe, K.M., Leneman, D., Lai, H.R., Cruce, P.R., Means, J.D., Johnson, C.L., Mittelholz, A., Joy, S.P., Chi, P.J., Mikellides, I.G., Carpenter, S., Navarro, S., Sebastian, E., Gomez-Elvira, J., Torres, J., Mora, L., Peinado, V., Lepinette, A., Hurst, K., Lognonné, P., Smrekar, S.E., & Banerdt, W.B. (2018). InSight Auxiliary Payload Sensor Suite (APSS). *Space Science Reviews*, 215(1), 4. http://dx.doi.org/10.1007/s11214-018-0570-x.

Banin, A., Clark, B.C., & Wankë, H. (1992). Surface chemistry and mineralogy. In H. H. Kieffer (Ed.), *MARS* (pp. 594-625). Tucson: University of Arizona Press.

Brinkman, N., Schmelzbach, C., Sollberger, D., Pierick, J., Edme, P., Haag, T., Kedar, S., Hudson, T., Andersson, F., van Driel, M., Stähler, S., Nicollier, T., Robertsson, J., Giardini, D., Spohn, T., Krause, C., Grott, M., Knollenberg, J., Hurst, K., Rochas, L., Vallade, J., Blandin, S., Lognonné, P., Pike, W.T., & Banerdt, W.B. (2022). In-situ regolith seismic velocity measurement at the InSight landing site on Mars. *Journal of Geophysical Research. Planets*, 127(10), e2022JE007229. http://dx.doi.org/10.1029/2022JE007229.

Butt, S.U., Antoine, J.F., & Martin, P. (2015). Simplified stiffness model for spherical rough contacts. *Tribology-Materials. Surfaces and Interfaces*, 9(2), 63-70. http://dx.doi.org/10.1179/1751584X15Y.0000000001.

Caicedo, B., Castillo-Betancourt, J.-P., Delage, B., Lognonné, P., & Banerdt, B. (2023). Wave velocities and Poisson ratio in a loose sandy martian regolith simulant under low stresses. Part 2: theoretical analysis. *Journal of Geophysical Research. Planets*, 128(11), e2023JE008008. http://dx.doi.org/10.1029/2023JE008008.

Castillo-Betancourt, J.-P., Delage, P., Caicedo, B., Lognonné, P., & Banerdt, B. (2023). Wave velocities and Poisson ratio in a loose sandy martian regolith simulant under low stresses. Part 1: laboratory investigation. *Journal of Geophysical Research. Planets*, 128(1), e2023JE007988. http://dx.doi.org/10.1029/2023JE007988.

Charalambous, C., McClean, J.B., Baker, M., Pike, W.T., Golombek, M., Lemmon, M., Ansan, V., Perrin, C., Spiga, A., Lorenz, R.D., Banks, M.E., Murdoch, N., Rodriguez, S., Weitz, C.M., Grant, J.A., Warner, N.H., Garvin, J., Daubar, I.J., Hauber, E., Stott, A.E., Johnson, C.L., Mittelholz, A., Warren, T., Navarro, S., Sotomayor, L.M., Maki, J., Lucas, A., Banfield, D., Newman, C., Viúdez-Moreiras, D., Pla-García, J., Lognonné, P., & Banerdt, W.B. (2021). Vortex-dominated aeolian activity at InSight's landing site, Part 1: multi-instrument observations, analysis and implications. *Journal of Physical Research: Planets*, 126(6), e2020JE006757. http://dx.doi.org/10.1029/2020JE006757.

Christensen, P.R., & Moore, H.J. (2008). The Martian surface layer. In H. H. Kieffer (Ed.), *MARS* (pp. 686-727). Tucson: University of Arizona Press.

Cooper, M.R., Kovach, R.L., & Watkins, J.S. (1974). Lunar near-surface structure. *Reviews of Geophysics*, 12(3), 291-308. http://dx.doi.org/10.1029/RG012i003p00291.

Dal Moro, G. (2015). Joint analysis of Rayleigh-wave dispersion and HVSR of lunar seismic data from the Apollo 14 and 16 sites. *Icarus*, 254, 338-349. http://dx.doi.org/10.1016/j.icarus.2015.03.017.

Delage, P., Karakostas, F., Dhemaied, A., Belmokhtar, M., Lognonné, P., Golombek, M., De Laure, E., Hurst, K., Dupla, J.-C., Kedar, S., Cui, Y.J., & Banerdt, B. (2017). An investigation of the mechanical properties of some Martian regolith simulants with respect to the surface properties at the InSight mission landing site. *Space Science Reviews*, 211(1-4), 191-213. http://dx.doi.org/10.1007/s11214-017-0339-7.

Delage, P., Castillo Betancourt, J.P., Caicedo Hormaza, B., Karakostas, F., De Laure, E., Lognonné, P., Antonangeli, D., & Banerdt, B. (2022). The interaction between the SEIS seismometer of the InSight Martian mission and a regolith simulant. *Géotechnique*, 74(1), 45-53. http://dx.doi.org/10.1680/jgeot.21.00171.

Ehlmann, B.L., Edgett, K.S., Sutter, B., Achilles, C.N., Litvak, M.L., Lapotre, M.G.A., Sullivan, R., Fraeman, A.A., Arvidson, R.E., Blake, D.F., Bridges, N.T., Conrad, P.G., Cousin, A., Downs, R.T., Gabriel, T.S.J., Gellert, R., Hamilton, V.E., Hardgrove, C., Johnson, J.R., Kuhn, S., Mahaffy, P.R., Maurice, S., McHenry, M., Meslin, P.-Y., Ming, D.W., Minitti, M.E., Morookian, J.M., Morris, R.V., O'Connell-Cooper, C.D., Pinet, P.C., Rowland, S.K., Schröder, S., Siebach, K.L., Stein, N.T., Thompson, L.M., Vaniman, D.T., Vasavada, A.R., Wellington, D.F., Wiens, R.C., & Yen, A.S. (2017). Chemistry, mineralogy, and grain properties at Namib and High dunes, Bagnold dune field, Gale crater, Mars: a synthesis of Curiosity rover observations. *Journal of Geophysical Research. Planets*, 122(12), 2510-2543. http://dx.doi.org/10.1002/2017JE005267.

Fayon, L., Knapmeyer-Endrun, B., Lognonné, P., Bierwirth, M., Kramer, A., Delage, P., Karakostas, F., Kedar, S., Murdoch, N., Garcia, R.F., Verdier, N., Tillier, S., Pike, W.T., Hurst, K., Schmelzbach, C., & Banerdt, W.B. (2018). A numerical model of the SEIS leveling system transfer matrix and resonances: application to SEIS rotational seismology and dynamic ground interaction. *Space Science Reviews*, 214(8), 119. http://dx.doi.org/10.1007/s11214-018-0555-9.

Folkner, W.M., Dehant, V., Le Maistre, S., Yseboodt, M., Rivoldini, A., van Hoolst, T., Asmar, S.W., & Golombek, M.P. (2018). The rotation and interior structure experiment on the InSight mission to Mars. *Space Science Reviews*, 214(5), 100. http://dx.doi.org/10.1007/s11214-018-0530-5.

Goetz, W., Pike, W.T., Hviid, S.F., Madsen, M.B., Morris, R.V., Hecht, M.H., Staufer, U., Leer, K., Sykulska, H., Hemmig, E., Marshall, J., Morookian, J.M., Parrat, D., Vijendran, S., Bos, B.J., El Maarry, M.R., Keller, H.U., Kramm, R., Markiewicz, W.J., Drube, L., Blaney, D., Arvidson, R.E., Bell III, J.F., Reynolds, R., Smith, P.H., Woida, P., Woida, R., & Tanner, R. (2010). Microscopy analysis of soils at the Phoenix landing site, Mars: classification of soil particles and description of their optical and magnetic properties. *Journal of Geophysical Research*, 115(E8), E00E22. http://dx.doi.org/10.1029/2009JE003437.

Golombek, M., Haldemann, A.F.C., Simpson, R.A., Fergason, R.L., Putzig, N.E., Arvidson, R.E., Bell III, J.F., & Mellon, M.T. (2008). Martian surface properties from joint analysis of orbital, Earth-based, and surface observations. In J. Bell (Ed.), *The Martian surface: composition, mineralogy and physical properties* (pp. 468-497). Cambridge: Cambridge University Press.

Golombek, M., Kipp, D., Warner, N., Daubar, I.J., Fergason, R., Kirk, R.L., Beyer, R., Huertas, A., Piqueux, S., Putzig, N.E., Campbell, B.A., Morgan, G.A., Charalambous, C., Pike, W.T., Gwinner, K., Calef, F., Kass, D., Mischna, M., Ashley, J., Bloom, C., Wigton, N., Hare, T., Schwartz, C., Gengl, H., Redmond, L., Trautman, M., Sweeney, J., Grima, C., Smith, I.B., Sklyanskiy, E., Lisano, M., Benardini, J., Smrekar, S., Lognonné, P., & Banerdt, W.B. (2017). Selection of the InSight landing site. *Space Science Reviews*, 211(1-4), 5-95. http://dx.doi.org/10.1007/s11214-016-0321-9.

Golombek, M., Grott, M., Kargl, G., Andrade, J., Marshall, J., Warner, N., Teanby, N.A., Ansan, V., Hauber, E., Voigt, J., Lichtenheldt, R., Knapmeyer-Endrun, B., Daubar, I.J., Kipp, D., Muller, N., Lognonné, P., Schmelzbach, C., Banfield, D., Trebi-Ollennu, A., Maki, J., Kedar, S., Mimoun, D., Murdoch, N., Piqueux, S., Delage, P., Pike, W.T., Charalambous, C., Lorenz, R., Fayon, L., Lucas, A., Rodriguez, S., Morgan, P., Spiga, A., Panning, M., Spohn, T., Smrekar, S., Gudkova, T., Garcia, R., Giardini, D., Christensen, U., Nicollier, T., Sollberger, D., Robertsson, J., Ali, K., Kenda, B., & Banerdt, W.B. (2018). Geology and physical properties investigations by the InSight lander. *Space Science Reviews*, 214(5), 84. http://dx.doi.org/10.1007/s11214-018-0512-7.

Golombek, M., Warner, N.H., Grant, J.A., Hauber, E., Ansan, V., Weitz, C.M., Williams, N., Charalambous, C., Wilson, S.A., DeMott, A., Kopp, M., Lethcoe-Wilson, H., Berger, L., Hausmann, R., Marteau, E., Vrettos, C., Trussell, A., Folkner, W., Le Maistre, S., Mueller, N., Grott, M., Spohn, T., Piqueux, S., Millour, E., Forget, F., Daubar, I., Murdoch, N., Lognonné, P., Perrin, C., Rodriguez, S., Pike, W.T., Parker, T., Maki, J., Abarca, H., Deen, R., Hall, J., Andres, P., Ruoff, N., Calef, F., Smrekar, S., Baker, M.M., Banks, M., Spiga, A., Banfield, D., Garvin, J., Newman, C.E., & Banerdt, W.B. (2020a). Geology of the InSight landing site on Mars. *Nature Communications*, 11(1), 1014. http://dx.doi.org/10.1038/s41467-020-14679-1.

Golombek, M., Williams, N., Warner, N.H., Parker, T., Williams, M.G., Daubar, I., Calef, F., Grant, J., Bailey, P., Abarca, H., Deen, R., Ruoff, N., Maki, J., McEwen, A., Baugh, N., Block, K., Tamppari, L., Call, J., Ladewig, J., Stoltz, A., Weems, W.A., Mora-Sotomayor, L., Torres, J., Johnson, M., Kennedy, T., & Sklyanskiy, E. (2020b). Location and setting of the Mars InSight lander, instruments, and landing site. *Earth and Space Science*, 7(10), e2020EA001248. http://dx.doi.org/10.1029/2020EA001248.

Golombek, M., Kass, D., Williams, N., Warner, N., Daubar, I., Piqueux, S., Charalambous, C., & Pike, W.T. (2020c). Assessment of InSight landing site predictions. *Journal of Geophysical Research. Planets*, 125(8), e2020JE006502. http://dx.doi.org/10.1029/2020JE006502.

Golombek, M., Charalambous, C., Pike, W.T., & Sullivan, R. (2020d). The origin of sand and dust on Mars: evidence from the InSight landing site. In *Proceedings of the 51st Lunar and Planetary Science Conference* (Abstract No. 2744), Houston, Texas.

Golombek, M., Hudson, T., Bailey, P., Balabanska, N., Marteau, E., Charalambous, C., Baker, M., Lemmon, M., White, B., Lorenz, R.D., Spohn, T., Maki, J., Kallemeyn, P., Garvin, J.B., Newman, C., Hurst, K., Murdoch, N., Williams, N., Banerdt, W.B., Lognonné, P., Delage, P., Lapeyre, R., Gaudin, E., Yana, C., Verdier, N., Panning, M., Trebi-Ollennu, A., Ali, K., Mittelholz, A., Johnson, C., Langlais, B., Warner, N., Grant, J., Daubar, I.J., Ansan, V., Vrettos, C., Spiga, A., Banfield, D., Gomez, A., Mishra, P., Dotson, R., Krause, C., Sainton, G., & Gabsi, T. (2023). Results from InSight Robotic Arm Activities. *Space Science Reviews*, 219(3), 20. http://dx.doi.org/10.1007/s11214-023-00964-0.

Grott, M., Spohn, T., Knollenberg, J., Krause, C., Scharringhausen, M., Wippermann, T., Smrekar, S.E., Hudson, T.L., & Banerdt, W.B. (2019). Calibration of the heat flow and physical properties package (HP^3) for the InSight Mars mission. *Earth and Space Science*, 6(12), 2556-2574. http://dx.doi.org/10.1029/2019EA000670.

Grott, M., Spohn, T., Knollenberg, J., Krause, C., Hudson, T.L., Piqueux, S., Müller, N., Golombek, M., Vrettos, C., Marteau, E., Nagihara, S., Morgan, P., Murphy, J.P., Siegler, M., King, S.D., Smrekar, S.E., & Banerdt, W.B. (2021). Thermal conductivity of the Martian soil at the InSight landing site from HP^3 active heating experiments. *Journal of Geophysical Research. Planets*, 126(7), e2021JE006861. http://dx.doi.org/10.1029/2021JE006861.

Grott, M., Piqueux, S., Spohn, T., Knollenberg, J., Krause, C., Marteau, E., Hudson, T.L., Forget, F., Lange, L., Müller, N., Golombek, M., Nagihara, S., Morgan, P., Murphy, J.P., Siegler, M., King, S.D., Banfield, D., Smrekar, S.E., & Banerdt, W.B. (2023). Seasonal variations of soil thermal conductivity at the InSight landing site. *Geophysical Research Letters*, 50(7), e2021JE006861. http://dx.doi.org/10.1029/2023GL102975.

Haskin, L.A., Wang, A., Jolliff, B.L., McSween, H.Y., Clark, B.C., Des Marais, D.J., McLennan, S.M., Tosca, N.J., Hurowitz, J.A., Farmer, J.D., Yen, A., Squyres, S.W., Arvidson, R.E., Klingelhöfer, G., Schröder, C., Souza Junior, P.A., Ming, D.W., Gellert, R., Zipfel, J., Brückner, J., Bell III, J.F., Herkenhoff, K., Christensen, P.R., Ruff, S., Blaney, D., Gorevan, S., Cabrol, N.A., Crumpler, L., Grant, J., & Soderblom, L. (2005). Water alteration of rocks and soils from the Spirit rover site, Gusev crater, Mars. *Nature*, 436(7047), 66-69. http://dx.doi.org/10.1038/nature03640.

Herkenhoff, K.E., Golombek, M.P., Guiness, E.A., Johnson, J.B., Kusack, A., Richter, L., Sullivan, R.J., & Gorevan, S. (2008). In situ observations of the physical properties of the Martian surface. In J. Bell (Ed.), *The Martian surface: composition, mineralogy and physical properties* (pp. 451-467). Cambridge: Cambridge University Press. http://dx.doi.org/10.1017/CBO9780511536076.021.

Hurowitz, S., McLennan, S., Tosca, N., Arvidson, R.E., Michalski, J.R., Ming, D.W., Schröder, C., & Squyres, S.W. (2006). In situ and experimental evidence for acidic weathering of rocks and soils on Mars. *Journal of Geophysical Research*, 111(E2), E02S19. http://dx.doi.org/10.1029/2005JE002515.

Jamiolkowski, M. (2012). Role of Geophysical testing in geotechnical site characterization. *Soils and Rocks*, 35(2), 117-137. http://dx.doi.org/10.28927/SR.352117.

Johnson, D.M., Frisillo, A.L., Dorman, J., Latham, G.V., & Strangway, D. (1982). Compressional wave velocities of a lunar regolith sample in a simulated lunar environment. *Journal of Geophysical Research*, 87(B3), 1899-1902. http://dx.doi.org/10.1029/JB087iB03p01899.

Kedar, S., Andrade, J., Banerdt, B., Delage, P., Golombek, M., Grott, M., Hudson, T., Kiely, A., Knapmeyer, M., Knapmeyer-Endrun, B., Krause, C., Kawamura, T., Lognonne, P., Pike, T., Ruan, Y., Spohn, T., Teanby, N., Tromp, J., & Wookey, J. (2017). Analysis of regolith properties using seismic signals generated by InSight's HP^3 penetrator. *Space Science Reviews*, 211(1-4), 315-337. http://dx.doi.org/10.1007/s11214-017-0391-3.

Kolbuszewski, J.J. (1984). An experimental study of maximum and minimum porosities of sands. *Geotextiles and Geomembranes*, 1(2), 161-162.

Larose, E., Khan, A., Nakamura, Y., & Campillo, M. (2005). Lunar subsurface investigated from correlation of seismic noise. *Geophysical Research Letters*, 32(16), L16201. http://dx.doi.org/10.1029/2005GL023518.

Lognonné, P., Banerdt, W.B., Giardini, D., Pike, W.T., Christensen, U., Laudet, P., de Raucourt, S., Zweifel, P., Calcutt, S., Bierwirth, M., Hurst, K.J., Ijpelaan, F., Umland, J.W., Llorca-Cejudo, R., Larson, S.A., Garcia, R.F., Kedar, S., Knapmeyer-Endrun, B., Mimoun, D., Mocquet, A., Panning, M.P., Weber, R.C., Sylvestre-Baron, A., Pont, G., Verdier, N., Kerjean, L., Facto, L.J., Gharakanian, V., Feldman, J.E., Hoffman, T.L., Klein, D.B., Klein, K., Onufer, N.P., Paredes-Garcia, J., Petkov, M.P., Willis, J.R., Smrekar, S.E., Drilleau, M., Gabsi, T., Nebut, T., Robert, O., Tillier, S., Moreau, C., Parise, M., Aveni, G., Ben Charef, S., Bennour, Y., Camus, T., Dandonneau, P.A., Desfoux, C., Lecomte, B., Pot, O., Revuz, P., Mance, D., tenPierick, J., Bowles, N.E., Charalambous, C., Delahunty, A.K., Hurley, J., Irshad, R., Liu, H., Mukherjee, A.G., Standley, I.M., Stott, A.E., Temple, J., Warren, T., Eberhardt, M., Kramer, A., Kühne, W., Miettinen, E.-P., Monecke, M., Aicardi, C., André, M., Baroukh, J., Borrien, A., Bouisset, A., Boutte, P., Brethomé, K., Brysbaert, C., Carlier, T., Deleuze, M., Desmarres, J.M., Dilhan, D., Doucet, C., Faye, D., Faye-Refalo, N., Gonzalez, R., Imbert, C., Larigauderie, C., Locatelli, E., Luno, L., Meyer, J.-R., Mialhe, F., Mouret, J.M., Nonon, M., Pahn, Y., Paillet, A., Pasquier, P., Perez, G., Perez, R., Perrin, L., Pouilloux, B., Rosak, A., Savin de Larclause, I., Sicre, J., Sodki, M., Toulemont, N., Vella, B., Yana, C., Alibay, F., Avalos, O.M., Balzer, M.A., Bhandari, P., Blanco, E., Bone, B.D., Bousman, J.C., Bruneau, P., Calef, F.J., Calvet, R.J., D'Agostino, S.A., de los Santos, G., Deen, R.G., Denise, R.W., Ervin, J., Ferraro, N.W., Gengl, H.E., Grinblat, F., Hernandez, D., Hetzel, M., Johnson, M.E., Khachikyan, L., Lin, J.Y., Madzunkov, S.M., Marshall, S.L., Mikellides, I.G., Miller, E.A., Raff, W., Singer, J.E., Sunday, C.M., Villalvazo, J.F., Wallace, M.C., Banfield, D., Rodriguez-Manfredi, J.A., Russell, C.T., Trebi-Ollennu, A., Maki, J.N., Beucler, E., Böse, M., Bonjour, C., Berenguer, J.L., Ceylan, S., Clinton, J., Conejero, V., Daubar, I., Dehant, V., Delage, P., Euchner, F., Estève, I., Fayon, L., Ferraioli, L., Johnson, C.L., Gagnepain-Beyneix, J., Golombek, M., Khan, A., Kawamura, T., Kenda, B., Labrot, P., Murdoch, N., Pardo, C., Perrin, C., Pou, L., Sauron, A., Savoie, D., Stähler, S., Stutzmann, E., Teanby, N.A., Tromp, J., van Driel, M., Wieczorek, M., Widmer-Schnidrig, R., & Wookey, J. (2019). SEIS: InSight's Seismic Experiment for Internal Structure of Mars. *Space Science Reviews*, 215(1), 12. http://dx.doi.org/10.1007/s11214-018-0574-6.

Lognonné, P., Banerdt, W.B., Pike, W.T., Giardini, D., Christensen, U., Garcia, R.F., Kawamura, T., Kedar, S., Knapmeyer-Endrun, B., Margerin, L., Nimmo, F., Panning, M., Tauzin, B., Scholz, J.-R., Antonangeli, D., Barkaoui, S., Beucler, E., Bissig, F., Brinkman, N., Calvet, M., Ceylan, S., Charalambous, C., Davis, P., van Driel, M., Drilleau, M., Fayon, L., Joshi, R., Kenda, B., Khan, A., Knapmeyer, M., Lekic, V., McClean, J., Mimoun, D., Murdoch, N., Pan, L., Perrin, C., Pinot, B., Pou, L., Menina, S., Rodriguez, S., Schmelzbach, C., Schmerr, N., Sollberger, D., Spiga, A., Stähler, S., Stott, A., Stutzmann, E., Tharimena, S., Widmer-Schnidrig, R., Andersson, F., Ansan, V., Beghein, C., Böse, M., Bozdag, E., Clinton, J., Daubar, I., Delage, P., Fuji, N., Golombek, M., Grott, M., Horleston, A., Hurst, K., Irving, J., Jacob, A., Knollenberg, J., Krasner, S., Krause, C., Lorenz, R., Michaut, C., Myhill, R., Nissen-Meyer, T., ten Pierick, J., Plesa, A.-C., Quantin-Nataf, C., Robertsson, J., Rochas, L., Schimmel, M., Smrekar, S., Spohn, T., Teanby, N., Tromp, J., Vallade, J., Verdier, N., Vrettos, C., Weber, R., Banfield, D., Barrett, E., Bierwirth, M., Calcutt, S., Compaire, N., Johnson, C.L., Mance, D., Euchner, F., Kerjean, L., Mainsant, G., Mocquet, A., Rodriguez Manfredi, J.A., Pont, G., Laudet, P., Nebut, T., de Raucourt, S., Robert, O., Russell, C.T., Sylvestre-Baron, A., Tillier, S., Warren, T., Wieczorek, M., Yana, C., & Zweifel, P. (2020). Constraints on the shallow elastic and anelastic structure of Mars from InSight seismic data. *Nature Geoscience*, 13(3), 213-220. http://dx.doi.org/10.1038/s41561-020-0536-y.

Marteau, E., Golombek, M., Vrettos, C., Garvin, J.B., & Williams, N.R. (2021). Soil mechanical properties at the InSight landing site, Mars. In *Proceedings of the 52nd Lunar and Planetary Science Conference* (LPI Contrib., No. 2067), Houston, Texas.

Marteau, E., Golombek, M., Vrettos, C., Delage, P., Williams, N.R., & Ansan, V. (2022). Soil strength properties derived from scraping and dumping activities at the InSight landing site on Mars. In *Proceedings of the 53rd Lunar and Planetary Science Conference* (LPI Contrib., No. 1523), Houston, Texas.

Marteau, E., Golombek, M., Delage, P., Vrettos, C., Hurst, K., Gomez, A., Williams, N.R., Bailey, P., & Mishra, P. (2023). Initial results from the InSight lander robotic arm soil mechanics experiments on Mars. In *Proceedings of the 54th Lunar and Planetary Science Conference* (LPI Contrib., No. 2806), Houston, Texas.

McGlynn, I.O., Fedo, C.M., & McSween Junior, H.Y. (2011). Origin of basaltic soils at Gusev crater, Mars, by aeolian modification of impact-generated sediment. *Journal of Geophysical Research*, 116(E7), E00F22. http://dx.doi.org/10.1029/2010JE003712.

McGlynn, I.O., Fedo, C.M., & McSween Junior, H.Y. (2012). Soil mineralogy at the Mars Exploration Rover landing sites: an assessment of the competing roles of physical sorting and chemical weathering. *Journal of Geophysical Research*, 117(E1), E01006. http://dx.doi.org/10.1029/2011JE003861.

Mellon, M.T., Jakosky, B.M., Kieffer, H.H., & Christensen, P.R. (2000). High-resolution thermal inertia mapping from the Mars global surveyor thermal emission spectrometer. *Icarus*, 148(2), 437-455. http://dx.doi.org/10.1006/icar.2000.6503.

Minitti, M.E., Kah, L.C., Yingst, R.A., Edgett, K.S., Anderson, R.C., Beegle, L.W., Carsten, J.L., Deen, R.G., Goetz, W., Hardgrove, C., Harker, D.E., Herkenhoff, K.E., Hurowitz, J.A., Jandura, L., Kennedy, M.R., Kocurek, G., Krezoski, G.M., Kuhn, S.R., Limonadi, D., Lipkaman, L., Madsen, M.B., Olson, T.S., Robinson, M.L., Rowland, S.K., Rubin, D.M., Seybold, C., Schieber, J., Schmidt, M., Sumner, D.Y., Tompkins, V.V., van Beek, J.K., & Van Beek, T. (2013). MAHLI at the Rocknest sand shadow: science and science-enabling activities. *Journal of Physical Research: Planets*, 118(11), 2338-2360. http://dx.doi.org/10.1002/2013JE004426.

Moore, H.J., & Jakosky, B.M. (1989). Viking landing sites, remote sensing observations, and physical properties of Martian surface materials. *Icarus*, 81(1), 164-184. http://dx.doi.org/10.1016/0019-1035(89)90132-2.

Morgan, P., Grott, M., Knapmeyer-Endrun, B., Golombek, M., Delage, P., Lognonné, P., Piqueux, S., Daubar, I., Murdoch, N., Charalambous, C., Pike, W.T., Müller, N., Hagermann, A., Siegler, M., Lichtenheldt, R., Teanby, N., & Kedar, S. (2018). A pre-landing assessment of regolith properties at the InSight landing site. *Space Science Reviews*, 214(6), 104. http://dx.doi.org/10.1007/s11214-018-0537-y.

Mueller, N., Piqueux, S., Lemmon, M., Maki, J., Lorenz, R.D., Grott, M., Spohn, T., Smrekar, S.E., Knollenberg, J., Hudson, T.L., Krause, C., Millour, E., Forget, F., Golombek, M., Hagermann, A., Attree, N., Siegler, M., & Banerdt, W.B. (2021). Near surface properties of Martian regolith derived from InSight HP^3-RAD temperature observations during Phobos transits. *Geophysical Research Letters*, 48(15), e93542. http://dx.doi.org/10.1029/2021GL093542.

Murdoch, N., Mimoun, D., Garcia, R.F., Rapin, W., Kawamura, T., Lognonné, P., Banfield, D., & Banerdt, W.B. (2017a). Evaluating the wind-induced mechanical noise on the InSight seismometers. *Space Science Reviews*, 211(1-4), 419-455. http://dx.doi.org/10.1007/s11214-016-0311-y.

Murdoch, N., Kenda, B., Kawamura, T., Spiga, A., Lognonné, P., Mimoun, D., & Banerdt, W.B. (2017b). Estimations of the seismic pressure noise on Mars determined from Large Eddy Simulations and demonstration of pressure decorrelation techniques for the Insight mission. *Space Science Reviews*, 211(1-4), 457-483. http://dx.doi.org/10.1007/s11214-017-0343-y.

Nagihara, S., Ngo, P., & Grott, M. (2022). Thermal properties of the Mojave Mars Regolith simulant in Mars-like atmospheric conditions. *International Journal of Thermophysics*, 43(7), 98. http://dx.doi.org/10.1007/s10765-022-03023-y.

Palluconi, F.D., & Kieffer, H.H. (1981). Thermal inertia mapping of Mars from 60°S to 60°N. *Icarus*, 45(2), 415-426. http://dx.doi.org/10.1016/0019-1035(81)90044-0.

Pan, L., Quantin-Nataf, C., Tauzin, B., Michaut, C., Golombek, M., Lognonné, P., Grindrod, P., Langlais, B., Gudkova, T., Stepanova, I., Rodriguez, S., & Lucas, A. (2020). Crust stratigraphy and heterogeneities of the first kilometers at the dichotomy boundary in western Elysium Planitia and implications for InSight lander. *Icarus*, 338, 113511. http://dx.doi.org/10.1016/j.icarus.2019.113511.

Peters, G.H., Abbey, W., Bearman, G.H., Mungas, G.S., Smith, J.A., Anderson, R.C., Douglas, S., & Beegle, L.W. (2008). Mojave Mars simulant: characterization of a new geologic Mars analog. *Icarus*, 197(2), 470-479. http://dx.doi.org/10.1016/j.icarus.2008.05.004.

Pike, W.T., Staufer, U., Hecht, M.H., Goetz, W., Parrat, D., Sykulska-Lawrence, H., Vijendran, S., & Madsen, M.B. (2011). Quantification of the dry history of the Martian soil inferred from in situ microscopy. *Geophysical Research Letters*, 38(24), L24201. http://dx.doi.org/10.1029/2011GL049896.

Piqueux, S., Müller, N., Grott, M., Siegler, M., Millour, E., Forget, F., Lemmon, M., Golombek, M., Williams, N., Grant, J., Warner, N., Ansan, V., Daubar, I., Knollenberg, J., Maki, J., Spiga, A., Banfield, D., Spohn, T., Smrekar, S., & Banerdt, B. (2021). Regolith properties near the InSight Lander derived from 50 sols of radiometer measurements. *Journal of Geophysical Research. Planets*, 6(8), e2021JE006859. http://dx.doi.org/10.1029/2021JE006859.

Poganski, J., Kömle, N.I., Kargl, G., Schweiger, H.F., Grott, M., Spohn, T., Krömer, O., Krause, C., Wippermann, T., Tsakyridis, G., Fittock, M., Lichtenheldt, R., Vrettos, C., & Andrade, J.E. (2017). Extended pile driving model to predict the penetration of the InSight/HP^3 mole into the Martian soil. *Space Science Reviews*, 211(1-4), 217-236. http://dx.doi.org/10.1007/s11214-016-0302-z.

Presley, M.A., & Christensen, P.R. (1997). Thermal conductivity measurements of particulate materials 2. Results. *Journal of Geophysical Research*, 102(E3), 6551-6566. http://dx.doi.org/10.1029/96JE03303.

Putzig, N.E., & Mellon, M.T. (2007). Apparent thermal inertia and the surface heterogeneity of Mars. *Icarus*, 191(1), 68-94. http://dx.doi.org/10.1016/j.icarus.2007.05.013.

Santamarina, J.C., Klein, K.A., & Fam, M.A. (2001). S*oils and waves.* Chichester: Wiley.

Seiferlin, K., Ehrenfreund, P., Garry, J., Gunderson, K., Hütter, E., Kargl, G., Maturilli, A., & Merrison, J.P. (2008). Simulating Martian regolith in the laboratory. *Planetary and Space Science*, 56(15), 2009-2025. http://dx.doi.org/10.1016/j.pss.2008.09.017.

Sens-Schönfelder, C., & Larose, E. (2010). Lunar noise correlation, imaging and monitoring. *Earth Science*, 23(5), 519-530. http://dx.doi.org/10.1007/s11589-010-0750-6.

Sollberger, D., Schmelzbach, C., Andersson, F., Robertsson, J.O.A., Brinkman, N., Kedar, S., Banerdt, W.B., Clinton, J., van Driel, M., Garcia, R., Giardini, D., Grott, M., Haag, T., Hudson, T.L., Lognonné, P., Pierick, J., Pike, W., Spohn, T., Stähler, S.C., & Zweifel, P. (2021). A reconstruction algorithm for temporally aliased seismic signals recorded by the InSight Mars lander. *Earth and Space Science*, 8(8), e2020EA001234. http://dx.doi.org/10.1029/2020EA001234.

Spohn, T., Grott, M., Smrekar, S.E., Knollenberg, J., Hudson, T.L., Krause, C., Müller, N., Jänchen, J., Börner, A., Wippermann, T., Krömer, O., Lichtenheldt, R., Wisniewski, L., Grygorczuk, J., Fittock, M., Rheershemius, S., Spröwitz, T., Kopp, E., Walter, I., Plesa, A.C., Breuer, D., Morgan, P., & Banerdt, W.B. (2018). The heat flow and physical properties Package (HP^3) for the InSight mission. *Space Science Reviews*, 214(5), 96. http://dx.doi.org/10.1007/s11214-018-0531-4.

Spohn, T., Hudson, T.L., Marteau, E., Golombek, M., Grott, M., Wippermann, T., Ali, K.S., Schmelzbach, C., Kedar, S., Hurst, K., Trebi-Ollennu, A., Ansan, V., Garvin, J., Knollenberg, J., Müller, N., Piqueux, S., Lichtenheldt, R., Krause, C., Fantinati, C., Brinkman, N., Sollberger, D., Delage, P., Vrettos, C., Reershemius, S., Wisniewski, L., Grygorczuk, J., Robertsson, J., Edme, P., Andersson, F., Krömer, O., Lognonné, P., Giardini, D., Smrekar, S.E., & Banerdt, W.B. (2022a). The InSight HP^3 penetrator (mole) on Mars: soil properties derived from the penetration attempts and related activities. *Space Science Reviews*, 218(8), 72. http://dx.doi.org/10.1007/s11214-022-00941-z.

Spohn, T., Hudson, T., Witte, L., Wippermann, T., Wisniewski, L., Kedziora, B., Vrettos, C., Lorenz, R.D., Golombek, M., Lichtenheldt, R., Grott, M., Knollenberg, J., Krause, C., Fantinati, C., Nagihara, S., & Grygorczuk, J. (2022b). The InSight HP^3 mole on Mars: lessons learned from attempts to penetrate to depth in the Martian soil. *Advances in Space Research*, 69(8), 3140-3163. http://dx.doi.org/10.1016/j.asr.2022.02.009.

Stott, A.E., Charalambous, C., Warren, T.J., Pike, W.T., Myhill, R., Murdoch, N., McClean, J.B., Trebi-Ollennu, A., Lim, G., Garcia, R.F., Mimoun, D., Kedar, S., Hurst, K.J., Bierwirth, M., Lognonné, P., Teanby, N.A., Horleston, A., & Banerdt, W.B. (2021). The site tilt and lander transfer function from the short-period seismometer of InSight on Mars. *Bulletin of the Seismological Society of America*, 111(6), 2889-2908. http://dx.doi.org/10.1785/0120210058.

Tanimoto, T., Eitzel, M., & Yano, T. (2008). The noise cross-correlation approach for Apollo 17 LSPE data: diurnal change in seismic parameters in shallow lunar crust. *Journal of Geophysical Research*, 113(E8), E08011. http://dx.doi.org/10.1029/2007JE003016.

Terzaghi, K., & Peck, R.B. (1947). *Theoretical soil mechanics*. New York: Wiley.

Trebi-Ollennu, A., Kim, W., Ali, K., Khan, O., Sorice, C., Bailey, P., Umland, J., Bonitz, R., Ciarleglio, C., Knight, J., Haddad, N., Klein, K., Nowak, S., Klein, D., Onufer, N., Glazebrook, K., Kobeissi, B., Baez, E., Sarkissian, F., Badalian, M., Abarca, H., Deen, R.G., Yen, J., Myint, S., Maki, J., Pourangi, A., Grinblat, J., Bone, B., Warner, N., Singer, J., Ervin, J., & Lin, J. (2018). InSight Mars lander robotics instrument deployment system. *Space Science Reviews*, 214(5), 93. http://dx.doi.org/10.1007/s11214-018-0520-7.

Verdier, N., Ansan, V., Delage, P., Ali, K.S., Beucler, E., Charalambous, C., Constant, E., Spiga, A., Golombek, M., Marteau, E., Lapeyre, R., Gaudin, E., Yana, C., Hurst, K., Lognonné, P., & Banerdt, B.W. (2023). Using wind dispersion effects during the InSight tether burial activities to better constrain the regolith grain size distribution. *Journal of Geophysical Research. Planets*, 128(5), e2022JE007707. http://dx.doi.org/10.1029/2022JE007707.

Walton, O.R., De Moor, P.C., & Gill, K.S. (2007). Effects of gravity on cohesive behavior of fine powders: implications for processing Lunar regolith. *Granular Matter*, 9(5), 353-363. http://dx.doi.org/10.1007/s10035-006-0029-8.

Warner, N.H., Golombek, M.P., Sweeney, J., Fergason, R., Kirk, R., & Schwartz, C. (2017). Near surface stratigraphy and regolith production in southwestern Elysium Planitia, Mars: implications for Hesperian-Amazonian terrains and the InSight lander mission. *Space Science Reviews*, 211(1-4), 147-190. http://dx.doi.org/10.1007/s11214-017-0352-x.

Warner, N.H., Golombek, M.P., Ansan, V., Marteau, E., Williams, N., Grant, J.A., Hauber, E., Weitz, C., Wilson, S., Piqueux, S., Mueller, N., Grott, M., Spohn, T., Pan, L., Schmelzbach, C., Daubar, I.J., Garvin, J., Charalambous, C., Baker, M., & Banks, M. (2022). In situ and orbital stratigraphic characterization of the InSight landing site: the type example of a regolith-covered lava plain on Mars. *Journal of Geophysical Research. Planets*, 127(4), e2022JE007232. http://dx.doi.org/10.1029/2022JE007232.

Yen, A.S., Gellert, R., Schröder, C., Morris, R.V., Bell III, J.F., Knudson, A.T., Clark, B.C., Ming, D.W., Crisp, J.A., Arvidson, R.E., Blaney, D., Brückner, J., Christensen, P.R., DesMarais, D.J., Souza Júnior, P.A., Economou, T.E., Ghosh, A., Hahn, B.C., Herkenhoff, K.E., Haskin, L.A., Hurowitz, J.A., Joliff, B.L., Johnson, J.R., Klingelhöfer, G., Madsen, M.B., McLennan, S.M., McSween, H.Y., Richter, L., Rieder, R., Rodionov, D., Soderblom, L., Squyres, S.W., Tosca, N.J., Wang, A., Wyatt, M., & Zipfel, J. (2005). An integrated view of the chemistry and mineralogy of Martian soils. *Nature*, 436(7047), 49-54. http://dx.doi.org/10.1038/nature03637.